ORP5/8 and MIB/MICOS link ER-mitochondria and intra-mitochondrial contacts for non-vesicular transport of phosphatidylserine

Vera F Monteiro-Cardoso, Leila Rochin, Amita Arora, Audrey Houcine, Eeva Jääskeläinen, Annukka M Kivelä, Cécile Sauvanet, Romain Le Bars, Eyra Marien, Jonas Dehairs, et al.

Cell Reports

Article

ORP5/8 and MIB/MICOS link ER-mitochondria and intra-mitochondrial contacts for non-vesicular transport of phosphatidylserine

Graphical abstract

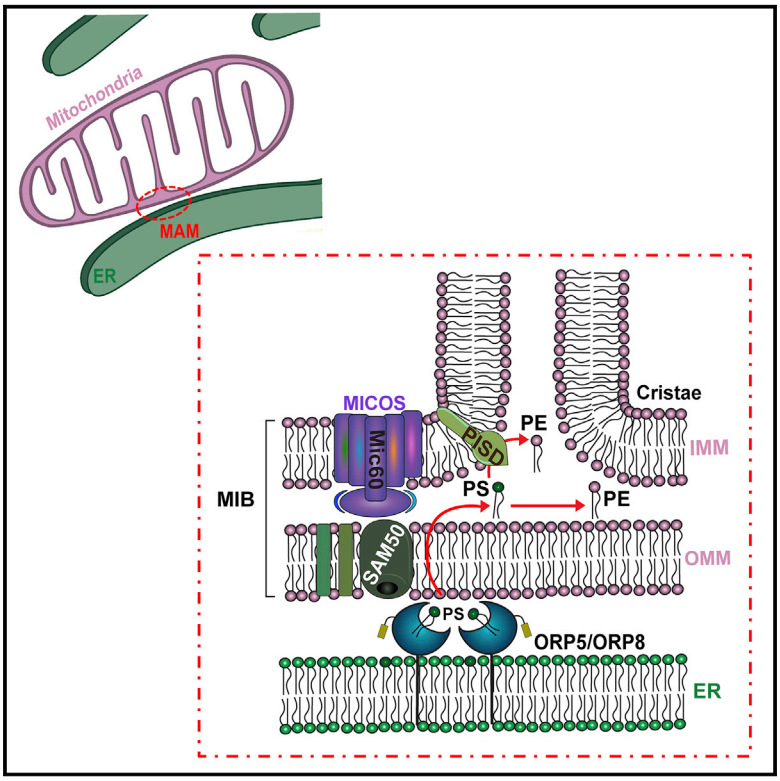

Highlights

- The endogenous ORP5 and ORP8 mainly localize and interact at MAM
- ORP5 and ORP8 interact with the mitochondrial MIB/MICOS complexes
- ORP5 and ORP8 mediate non-vesicular transport of PS from the ER to the mitochondria

Authors

Vera F. Monteiro-Cardoso, Leila Rochin, Amita Arora, ..., David Tareste, Vesa M. Olkkonen, Francesca Giordano

Correspondence

francesca.giordano@i2bc.paris-saclay.fr

In brief

In this study, Monteiro-Cardoso et al. reveal that the lipid transfer proteins ORP5/ORP8 are mainly localized at ER subdomains in contact with mitochondria. At these sites, ORP5/ORP8 interact and cooperate with the mitochondrial MIB/MICOS complexes to mediate non-vesicular transport of phosphatidylserine from the ER to mitochondria.

Monteiro-Cardoso et al., 2022, Cell Reports *40*, 111364
September 20, 2022
https://doi.org/10.1016/j.celrep.2022.111364

CellPress

Cell Reports

CellPress
OPEN ACCESS

Article

ORP5/8 and MIB/MICOS link ER-mitochondria and intra-mitochondrial contacts for non-vesicular transport of phosphatidylserine

Vera F. Monteiro-Cardoso,[1,2,10] Leila Rochin,[1,2,10] Amita Arora,[3] Audrey Houcine,[4] Eeva Jääskeläinen,[3] Annukka M. Kivelä,[3] Cécile Sauvanet,[1,2] Romain Le Bars,[1,6] Eyra Marien,[5] Jonas Dehairs,[5] Julie Neveu,[1,2] Naima El Khallouki,[1,2] Elena Santonico,[7] Johannes V. Swinnen,[5] David Tareste,[8] Vesa M. Olkkonen,[3,9] and Francesca Giordano[1,2,11,*]

[1]Institute for Integrative Biology of the Cell (I2BC), CEA, CNRS, Université Paris-Saclay, 91198 Gif-sur-Yvette Cedex, France
[2]Inserm U1280, 91198 Gif-sur-Yvette Cedex, France
[3]Minerva Foundation Institute for Medical Research, Biomedicum 2U, 00290 Helsinki, Finland
[4]Institut Jacques Monod, CNRS, UMR7592, Université Paris Diderot, Sorbonne Paris Cité, 75013 Paris, France
[5]Laboratory of Lipid Metabolism and Cancer, Department of Oncology, KU Leuven, 3000 Leuven, Belgium
[6]Imagerie-Gif, Light Microscopy Facility, Institute for Integrative Biology of the Cell (I2BC), CEA, CNRS, Université Paris-Saclay, 91198 Gif-sur-Yvette Cedex, France
[7]University of Rome Tor Vergata, via della ricerca scientifica, dipartimento di Biologia, 00133 Roma RM, Italy
[8]Université Paris Cité, Inserm UMR-S 1266, Institute of Psychiatry and Neuroscience of Paris (IPNP), Paris, France
[9]Department of Anatomy, Faculty of Medicine, University of Helsinki, 00014 Helsinki, Finland
[10]These authors contributed equally
[11]Lead contact
*Correspondence: francesca.giordano@i2bc.paris-saclay.fr
https://doi.org/10.1016/j.celrep.2022.111364

SUMMARY

Mitochondria are dynamic organelles essential for cell survival whose structural and functional integrity rely on selective and regulated transport of lipids from/to the endoplasmic reticulum (ER) and across the mitochondrial intermembrane space. As they are not connected by vesicular transport, the exchange of lipids between ER and mitochondria occurs at membrane contact sites. However, the mechanisms and proteins involved in these processes are only beginning to emerge. Here, we show that the main physiological localization of the lipid transfer proteins ORP5 and ORP8 is at mitochondria-associated ER membrane (MAM) subdomains, physically linked to the mitochondrial intermembrane space bridging (MIB)/mitochondrial contact sites and cristae junction organizing system (MICOS) complexes that bridge the two mitochondrial membranes. We also show that ORP5/ORP8 mediate non-vesicular transport of phosphatidylserine (PS) lipids from the ER to mitochondria by cooperating with the MIB/MICOS complexes. Overall our study reveals a physical and functional link between ER-mitochondria contacts involved in lipid transfer and intra-mitochondrial membrane contacts maintained by the MIB/MICOS complexes.

INTRODUCTION

Vesicular trafficking is the major pathway for transport of proteins and lipids between membranes. However, an alternative route, which is vesicle independent, occurs at regions of close inter-organelle membrane proximity (within less than 30 nm), also called membrane contact sites (Scorrano et al., 2019). This route is particularly important to preserve membrane composition, integrity, and identity of intracellular organelles such as mitochondria that are largely excluded from the classical vesicle-mediated trafficking pathway. Like other organelles, mitochondria can be closely associated with the endoplasmic reticulum (ER), the major site of lipid synthesis and the major intracellular calcium (Ca^{2+}) store. ER membrane subdomains closely apposed to mitochondria are called mitochondria-associated ER membranes (MAMs) and they facilitate the exchange of Ca^{2+} and lipids between the two organelles (Herrera-Cruz and Simmen, 2017; Tatsuta et al., 2014; Vance, 2014).

Mitochondria are involved in a plethora of cellular processes, including energy production, lipid metabolism, Ca^{2+} homeostasis, and apoptosis. To fulfill their numerous functions, mitochondria need to maintain a defined membrane composition by receiving essential lipids and lipid precursors from the ER through membrane contact sites (Acoba et al., 2020; Giordano, 2018; Vance and Tasseva, 2013).

Increasing lines of evidence suggest that lipid transfer proteins (LTPs) play a major role in regulating the lipid composition of membranous organelles by facilitating non-vesicular lipid transport at membrane contact sites. In recent years, several tethering complexes with lipid transfer activity have been identified

at membrane contact sites between the ER and other intracellular organelles as well as the plasma membrane (PM) in yeast and mammalian cells (Wong et al., 2019). However, our knowledge of how lipids are exchanged at ER-mitochondria membrane contact sites remains rudimentary, and the LTPs that localize and function at these sites are just starting to be discovered. The best-studied lipid transfer/tethering complex at ER-mitochondria contact sites is the yeast ER-mitochondria encounter structure (ERMES) (Kornmann et al., 2009, Lang et al., 2015), which bridges the ER and the mitochondrial membranes and also facilitates the exchange of phospholipids (in particular phosphatidylcholine [PC]) between them (Kawano et al., 2018). In metazoans, very little is known on how lipids are exchanged at ER-mitochondria membrane contact sites and about the proteins involved in this process. Some tethering proteins at mammalian ER-mitochondria contact sites have emerged in recent years, such as VDAC-GRP75-IP3R and PTPIP51-VAPB complexes (Gatta and Levine, 2017). A recent study has proposed that PTPIP51 could regulate cardiolipin levels by transferring its precursor phosphatidic acid (PA) to the mitochondria via its TPR domain (Yeo et al., 2021). However, further work is required to clarify the lipid transfer ability of the PTPIP51 TPR domain (Giordano and Prodromou, 2021). Also, recently, mammalian LTPs with tethering function, such as VPS13A or Pdzd8 (the latter being proposed as a paralog of the ERMES subunit Mmm1; Wideman et al., 2018), were shown to localize at membrane contact sites, including those between ER and mitochondria, where they regulate membrane tethering and, in the case of Pdzd8, mitochondrial Ca^{2+} uptake (Hirabayashi et al., 2017; Kumar et al., 2018). However, a direct involvement of these proteins in non-vesicular lipid transport between ER and mitochondrial membranes remains to be proved.

The oxysterol-binding protein (OSBP)-related proteins constitute a large family of LTPs conserved from yeast (Osh) to humans (ORP) and localized to different subcellular sites, shown in several cases to be membrane contact sites. A common feature of all ORPs is the presence of an OSBP-related lipid-binding/transfer (ORD) domain. Most ORP proteins contain a two phenylalanines (FF) in an acidic tract (FFAT) motif that binds ER-localized VAP proteins and a pleckstrin homology (PH) domain that interacts with lipids or proteins in distinct non-ER organelle membranes. Two members of this family, ORP5 and ORP8, do not contain an FFAT motif but are directly anchored to the ER through a C-terminal transmembrane (TM) segment (Olkkonen, 2015).

ORP5 and ORP8 have previously been shown to localize at ER-PM contact sites where they transfer phosphatidylserine (PS) from the cortical ER to the PM, in counter-exchange with the phosphoinositides phosphatidylinositol-4-phosphate (PI4P) and phosphatidylinositol 4,5-bisphosphate (PIP_2) (Chung et al., 2015; Ghai et al., 2017). We have shown before that ORP5 and ORP8 are also present in the MAM and play a key role in maintaining mitochondrial integrity (Galmes et al., 2016). We and others have also shown that ORP5 and ORP8 form a protein complex in the cell (Chung et al., 2015; Galmes et al., 2016). However, ORP5 and ORP8, when overexpressed, display a different distribution within membrane contact sites. In particular, overexpression of ORP5 greatly expands ER-PM contacts (Chung et al., 2015; Galmes et al., 2016), resulting in an accumulation of ORP5 at these sites, while overexpressed ORP8 is largely retained in the reticular ER. As all the studies on ORP5 and ORP8 so far have employed their individual overexpression, the endogenous sites where ORP5 and ORP8 interact and function as a complex are still unknown.

Interestingly, transport of PS is a key event occurring at ER-mitochondria contact sites. Newly synthesized PS, by the ER-localized PS-synthase 1 (PSS1), is shuttled from the ER to the outer mitochondrial membrane (OMM) and from OMM to inner mitochondrial membrane (IMM), where it is rapidly converted to phosphatidylethanolamine (PE) by the PS-decarboxylase enzyme PISD (Tamura et al., 2020; Vance, 2014; Vance and Tasseva, 2013). At the IMM, PE plays crucial roles in maintaining mitochondrial tubular morphology and therefore mitochondrial respiratory functions (Joshi et al., 2012; Steenbergen et al., 2005). Regardless of extensive studies on PS transport between ER and mitochondria since its first discovery 32 years ago (Vance, 1990), the underlying mechanisms and proteins involved are still elusive.

Membrane contact sites also exist between the OMM and the IMM and are mediated by the mitochondrial intermembrane space bridging (MIB) and mitochondrial contact sites and cristae junction organizing system (MICOS) complexes. The MICOS complex is a multi-subunit complex preferentially located at cristae junctions (CJs), tubular structures that connect the IMM to the cristae, and it is necessary for CJ formation, cristae morphology, and mitochondria function (Friedman et al., 2015; Hoppins et al., 2011; Huynen et al., 2016; von der Malsburg et al., 2011; Wollweber et al., 2017). The integral IMM protein Mic60 is the central component of the MICOS complex and carries a large domain exposed to the mitochondria intermembrane space (IMS) that interacts with the OMM sorting and assembly machinery (SAM) to form the MIB complex (Harner et al., 2011; Korner et al., 2012; Ott et al., 2012; van der Laan et al., 2016; von der Malsburg et al., 2011). The SAM complex is constituted of SAM50 (a pore-forming β barrel protein), metaxin 1 and 2, and is involved in the membrane insertion and assembly of mitochondrial β barrel proteins (Hohr et al., 2018; Kozjak et al., 2003; Kozjak-Pavlovic et al., 2007). However, whether and how OMM-IMM contact sites are linked to ER-mitochondria contacts in mammalian cells is still largely unknown.

Here we uncover the endogenous localization of ORP5 and ORP8, revealing that the major sites of their interaction in physiological conditions are the MAMs. We also show that the ER subdomains where ORP5 and ORP8 reside are physically connected to the intra-mitochondrial membrane contacts bridged by the MIB/MICOS complexes at CJs. We then show that ORP5/8 cooperate with SAM50 and Mic60, key components of the MIB/MICOS complex, to mediate PS transport from the ER to the mitochondrial membranes at ER-mitochondria contact sites in mammalian cells, and consequently the synthesis of mitochondrial PE.

Our findings thus reveal a tripartite association between the ER and the two mitochondrial membranes that links lipid transfer across these membranes, cristae biogenesis, and consequently mitochondria function.

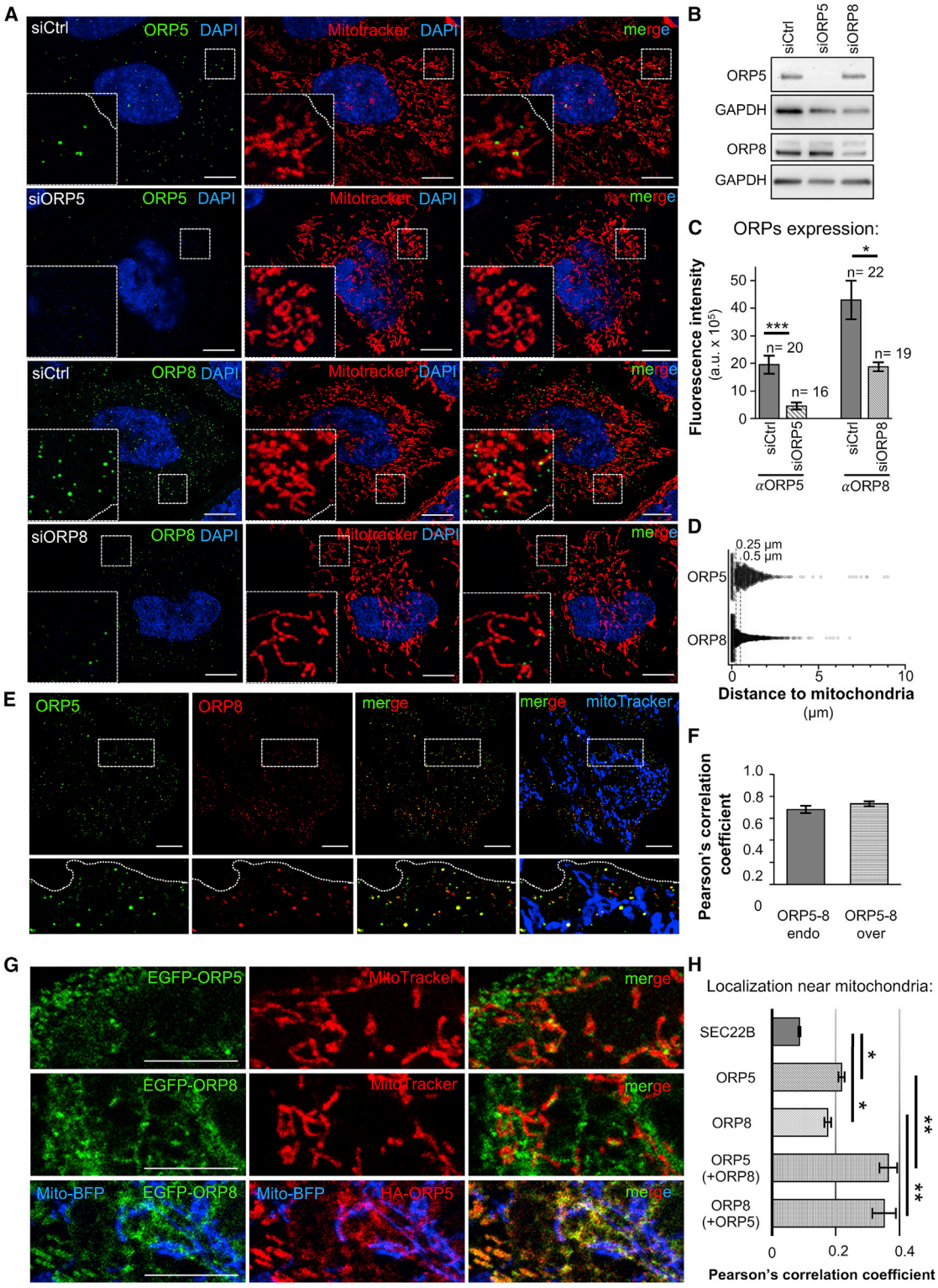

Figure 1. Endogenous and co-overexpressed ORP5 and ORP8 co-localize at ER-mitochondria contact sites

(A) Confocal images of Ctrl, ORP5, and ORP8 knockdown HeLa cells immunostained using anti-ORP5 or ORP8 antibodies (green), and treated with MitoTracker to label mitochondria (red) and DAPI to stain the nuclei (blue). Images are presented as individual layers. Insets show magnifications of the boxed regions. Note the close association of endogenous ORP5 and ORP8 to mitochondria. Scale bar, 10 μm.

(B) WB analysis showing ORP5, ORP8, and GAPDH levels in protein lysates from Ctrl, ORP5, and ORP8 knockdown HeLa cells.

(legend continued on next page)

RESULTS

ER-mitochondria contact sites are the main localization of the ORP5-ORP8 complex

The localization of ORP5 and ORP8 at endogenous level is still unknown. We thus investigated their endogenous localization by immunofluorescence (IF) using antibodies against ORP5 and ORP8 proteins. First, we validated the specificity of these antibodies in cells overexpressing ORP5 or ORP8 proteins fused with a similar fluorescent tag (EGFP-ORP5 or EGFP-ORP8) and found that ORP5 and ORP8 signals detected using these antibodies co-localized with the overexpressed proteins (Figures S1A and S1B). Then, we analyzed ORP5 and ORP8 endogenous localization in control HeLa cells and in cells where ORP5 and ORP8 were downregulated by RNAi and whose mitochondria were labeled by MitoTracker. We found a strong decrease in ORP5 and ORP8 IF labeling upon their knockdown (KD) (Figures 1A and 1C and S1F), whose efficiency was confirmed by western blotting (WB) (Figures 1B and S1C–S1F), validating the specificity of the used antibodies. ORP5 and ORP8-positive compartments in control conditions overlapped with the ER protein RFP-Sec22b, confirming endogenous ORP5 and ORP8 localization to the ER (Figure S2A). Interestingly, the majority of endogenous ORP5 and ORP8 co-localized to subcellular compartments in close proximity to mitochondria (Figures 1A and 1D and 1E–1F).

We then sought to analyze ORP5 and ORP8 localization when co-overexpressed (at similar levels) by co-transfecting HA-ORP5 and EGFP-ORP8 in HeLa cells and comparing their localization with the individually expressed EGFP-ORP5 and EGFP-ORP8 by confocal microscopy. When expressed alone, EGFP-ORP5 localizes to ER in contact with mitochondria but also strongly increases ER-PM contact sites where it relocates, while it localizes very little in the reticular ER (Figures 1G and S2B; Galmes et al., 2016). Instead, EGFP-ORP8, when expressed alone, localizes mostly to ER-mitochondria contacts and to reticular ER, with only a minor pool at cortical ER (Figures 1G and S2B). Remarkably, even if the individually overexpressed ORP5 and ORP8 were differently distributed among membrane contact sites, their localization at ER-mitochondria contacts was higher compared with a general ER protein, such as Sec22b (Figure 1H). Moreover, and interestingly, when expressed together, ORP5 and ORP8 equally redistributed and co-localized to cortical ER, reticular ER, and ER-mitochondria contacts (Figures 1G and S2B). In particular, their localization to ER-mitochondria contacts was higher compared with when expressed individually (Figure 1H). Also, the co-localization of co-overexpressed ORP5 and ORP8 was comparable with the co-localization of the endogenous proteins, as revealed by the high Pearson's correlation coefficient, which, in both cases, was close to 1 (Figure 1F). These data indicate that co-expression of ORP5 and ORP8 mimics the physiological localization of these proteins as a complex, when the expression level of one of the two proteins is not highly enriched compared with the other.

To further quantify ORP5 and ORP8 co-localization and interaction at ER-mitochondria contact sites in co-overexpression and endogenous conditions, we used Duolink-Proximity Ligation Assay (PLA) coupled with staining of mitochondria (MitoTracker) and confocal microscopy. PLA signals corresponding to ORP5-ORP8 interaction were observed throughout the cell in both endogenous and co-overexpression (HA-ORP5 and 3XFLAG-ORP8) conditions (Figure 2A). The specificity of this assay and of the antibodies used was confirmed by the strong decrease in PLA signals for endogenous ORP5-ORP8 interaction in cells with ORP5 and ORP8 knocked down (Figures 2B and S3A). Likewise, a significant increase in ORP5-ORP8 PLA signals was induced by the overexpression of these proteins (Figure 2B).

Close association of PLA spots to mitochondria, indicating localization at ER-mitochondria contact sites, was measured after segmentation of the mitochondrial network by Imaris (Figure 2A, right panel; S3b). Interestingly, the majority of ORP5-ORP8 PLA signals localized at ER-mitochondria contact sites (52% of endogenous ORP5-ORP8 and 50% of co-overexpressed ORP5-ORP8) (Figures 2A and 2C). The localization of ORP5-ORP8 PLA signals to ER-PM contact sites was analyzed in HeLa cells transfected with RFP-PH-PLCδ, to stain the PM, and Mito-BFP, to label mitochondria. However, only a minor pool of ORP5-8 PLA spots was found in contact with the PM (4% of endogenous ORP5-ORP8 and 5% of co-overexpressed ORP5-ORP8) (Figures 2D–2F). The localization of ORP5-ORP8 PLA spots to the ER, including MAMs, was confirmed in cells co-expressing the ER protein Sec22b and the mitochondrial-targeted Mito-BFP (Figure S3C).

Overall, these data reveal that the main sites where ORP5 and ORP8 localize and interact in endogenous physiological

(C) Quantification of ORP5 and ORP8 fluorescent intensity in Ctrl, ORP5, and ORP8 knockdown cells. Mean of fluorescent intensities in arbitrary units (a.u. × 10^5). Error bars denote ± standard error of the mean (SEM). Number of cells given above bars. Statistical analysis: p values were determined by unpaired Student's t test, *$p < 0.05$, ***$p < 0.001$.

(D) Distribution of ORP5 and ORP8 by IF staining (spots) in relation to their distance (μm) to mitochondria indicating that part of the endogenous ORP5 and ORP8 in the cell is detected in close proximity to mitochondria (<0.5 μm).

(E) Confocal images of a HeLa cell immunostained using anti-ORP5 (green) or ORP8 (red) antibodies and MitoTracker (blue). Images are presented as individual layers. Insets show magnifications of the boxed regions. Scale bar, 10 μm.

(F) Quantification of the co-localization (Pearson's factor) of ORP5-ORP8 in endogenous (ORP5-8 end) and co-overexpression (ORP5-8 over) conditions. Bars indicate mean values ±SEM. Number of cell analyzed: ORP5-8 end (n = 15), ORP5-8 over (n = 14).

(G) Confocal micrograph of a region of HeLa cell (zoomed from Figure S2B) transfected with EGFP-ORP5 (green), EGFP-ORP8 (green), or EGFP-ORP8 (green) + HA-ORP5 (anti-HA, red), and with Mito-BFP (blue). Scale bar, 10 μm.

(H) Quantifications of the association to mitochondria (Pearson's factor) of the indicated EGFP-tagged constructs. Bars indicate mean values ±SEM of three independent experiments with 10 cells per sample analyzed in each experiment (n = 30). Statistical analysis: unpaired Student's t test comparing EGFP-ORP5 (ORP5) or EGFP-ORP8 (ORP8) with EGFP-Sec22b (SEC22b) and HA-ORP5 (+EGFP-ORP8) or EGFP-ORP8 (+HA-ORP5) to EGFP-ORP5 or EGFP-ORP8, respectively. *$p < 0.05$, **$p < 0.01$.

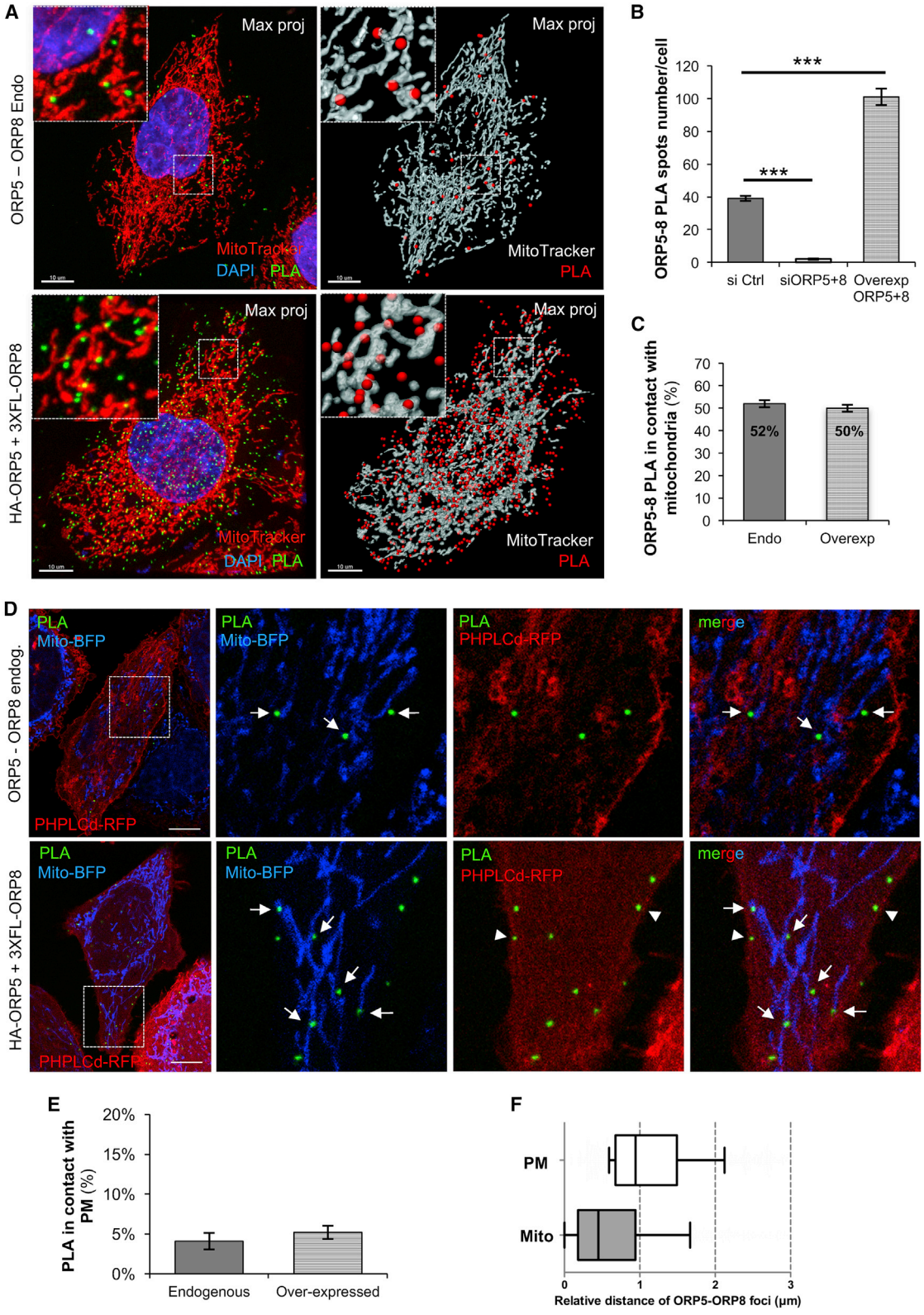

(legend on next page)

conditions are the ER-mitochondria contact sites, and not the ER-PM contact sites.

ORP5 and ORP8 physically interact with the MIB complex facing CJs

To investigate whether ORP5/8 localize to specific ER-mitochondria contact subdomains, we performed a morphological analysis of ORP5 localization by immuno-electron microscopy (IEM) on ultrathin cryosections from HeLa cells transfected with HA-ORP5 or EGFP-ORP5 (as endogenous ORP5/8 levels are too low to be detected by IEM). We previously reported that about 20% of ORP5 or ORP8 gold particles were associated to ER-mitochondria contact sites when individually expressed (Galmes et al., 2016). The advantage of analyzing ORP5 localization is its preferential localization to contact sites (20% at ER-mitochondria contacts and 60% at ER-PM contacts), when expressed alone, compared with ORP8, which also remains largely present within the reticular ER (60% of ORP8 versus 20% of ORP5) (Galmes et al., 2016). Interestingly, the majority of ORP5 gold particles at ER-mitochondria contact sites were found to localize to ER elements in a very close proximity (86% within 0–100 nm, 50% of which within 50 nm) to the CJ (arrow, Figures 3A and 3B), tubular structures that connect the IMM to the cristae. To exclude that ORP5 localization near CJ was not a consequence of its distribution throughout the ER membranes, we sought to determine if other ER proteins had a similar frequency of proximity to CJ. Thus, we compared ORP5 localization to Sec61β, an ER protein present in ER elements widely distributed throughout the cells and very little at ER-mitochondria contacts (Galmes et al., 2016). Co-immunolabeling of EGFP-ORP5 or EGFP-Sec61β and the luminal ER protein disulfide isomerase (PDI) confirmed ORP5 localization to ER elements close to CJ (arrow, Figure 3C) but not of Sec61β, the bulk of which localized on ER membranes distant from the CJ (0% within 0–100 nm and 69% > 200 nm) even when close to mitochondria (Figure 3B and arrowheads in Figure 3C). To determine whether other contact site proteins would be similarly enriched at CJ, we analyzed the localization of PTPIP51, a mitochondrial tether known to localize at ER-mitochondria contact sites (Stoica et al., 2014) and also a binding partner of ORP5/8 (Galmes et al., 2016). A small pool of PTPIP51-HA could be detected near CJ where they co-localized with EGFP-ORP8 or EGFP-ORP5. However, the majority of PTPIP51 randomly distributed throughout the mitochondrial surface (Figures 3D and 3E). Hence, our results support the conclusion that ORP5/8 specifically localize to ER-mitochondria contact sites closely associated to CJ. Interestingly, in yeast, CJs were shown to be closely associated to OMM-IMM contact sites tethered by the MICOS complex (Harner et al., 2011). IEM analysis using Mic60-EGFP, an EGFP-tagged construct of the human orthologue of the central component of the MICOS complex, confirmed that human Mic60, similarly to its yeast orthologue, preferentially localizes to the IMM in close proximity to CJ and in the cristae that arise from them (arrow, Figure 3A). These results suggest that ER-mitochondria contact sites where ORP5/8 localize could be physically connected to the intra-mitochondrial membrane contact sites near CJ.

To identify binding partners of ORP5/8 at ER-mitochondria contact sites, we carried out a mass spectrometry (MS)-analysis on GFP pull-downs from cells expressing EGFP-ORP5, EGFP-ORP5ΔPH (an ORP5 variant lacking the PM-targeting PH domain that is localized at ER-mitochondria but not at ER-PM contact sites) or EGFP alone as a control (Figures 4A and S4A). As expected, the highest hit detected in both EGFP-ORP5 and EGFP-ORP5ΔPH pull-downs was ORP8. In accord with our previous study (Galmes et al., 2016), the mitochondrial protein PTPIP51 was also detected in the MS analysis. Interestingly, several new OMM proteins (listed in Figure 4A) were also found as major hits. Among these proteins, the MIB component SAM50 and the MICOS central subunit Mic60, binding partner of SAM50 at OMM-IMM contact sites (Ott et al., 2015; Tang et al., 2020), had the highest scores (Figure 4A). Interestingly, SAM50 and Mic60 showed a higher interaction score in EGFP-ORP5ΔPH immunoprecipitates compared with EGFP-ORP5. WB analysis using anti-actin as loading control showed that EGFP-ORP5ΔPH overexpression did not alter the amount of SAM50 and Mic60 proteins compared with the overexpression of either EGFP-ORP5 or EGFP alone (Figure S4D), indicating that the higher interaction scores of these proteins in the EGFP-ORP5ΔPH immunoprecipitates were not due to their increased levels. Of note, metaxin 2 was also detected in the MS of immunoprecipitated EGFP-ORP5 and EGFP-ORP5ΔPH,

Figure 2. The main localization of the endogenous ORP5-ORP8 complex is ER-mitochondria contact sites

(A) Representative confocal images of ORP5-ORP8 interaction in HeLa cells detected by Duolink PLA (green spots) in endogenous (ORP5-ORP8 Endo) and overexpressing (HA-ORP5 + 3xFL-ORP8) conditions, and their respective 3D representation by Imaris. Images are presented as maximum projection of all layers. Insets show magnifications of the boxed regions. Scale bar, 10 μm.

(B) Quantification of the number of ORP5-ORP8 PLA interactions in control (siCtrl, n = 39 cells), ORP5 and ORP8 knockdown (siORP5+8, n = 38 cells), and in overexpression of ORP5 and ORP8 (Ovrexp ORP5+8, n = 35 cells), showing that the downregulation or the upregulation of both ORP5 and ORP8, respectively, reduces and increases the number of interactions established between these two proteins. Statistical analysis: p values were determined by unpaired Student's t test, ***$p < 0.001$.

(C) Quantification of ORP5-ORP8 PLA interaction localized to ER-mitochondria contact sites in control (Endo, n = 33) and HeLa cells overexpressing ORP5 and ORP8 (HA-ORP5 + 3xFL-ORP8, n = 27 cells) showing that about 50% of ORP5-ORP8 interactions occurs at MAM.

(D) Representative confocal images of ORP5-ORP8 PLA interaction (green spots) detected in HeLa cells overexpressing PHPLCd-RFP, Mito-BFP (ORP5-ORP8 Endo), or in HeLa cells overexpressing PHPLCd-RFP, Mito-BFP, ORP5, and ORP8 (HA-ORP5 + 3xFL-ORP8). Images are presented as individual layers. Scale bar, 10 μm.

(E) Quantification of ORP5-ORP8 PLA signal localized to ER-plasma membrane (PM) contact sites indicate that about 5% of the total ORP5-ORP8 interactions occur to these subdomains of the ER membranes, in both control (endogenous, n = 6 cells) and HeLa cells overexpressing ORP5 and ORP8 (overexpressed, n = 14 cells).

(F) Box plot of ORP5-ORP8 endogenous PLA spots distance (μm) to mitochondria and PM (box around median value, whiskers 10%–90%) showing that the majority of ORP5-ORP8 interactions were detected in a close proximity to mitochondria (<0.38 μm) and distant from the PM (≥0.38 μm).

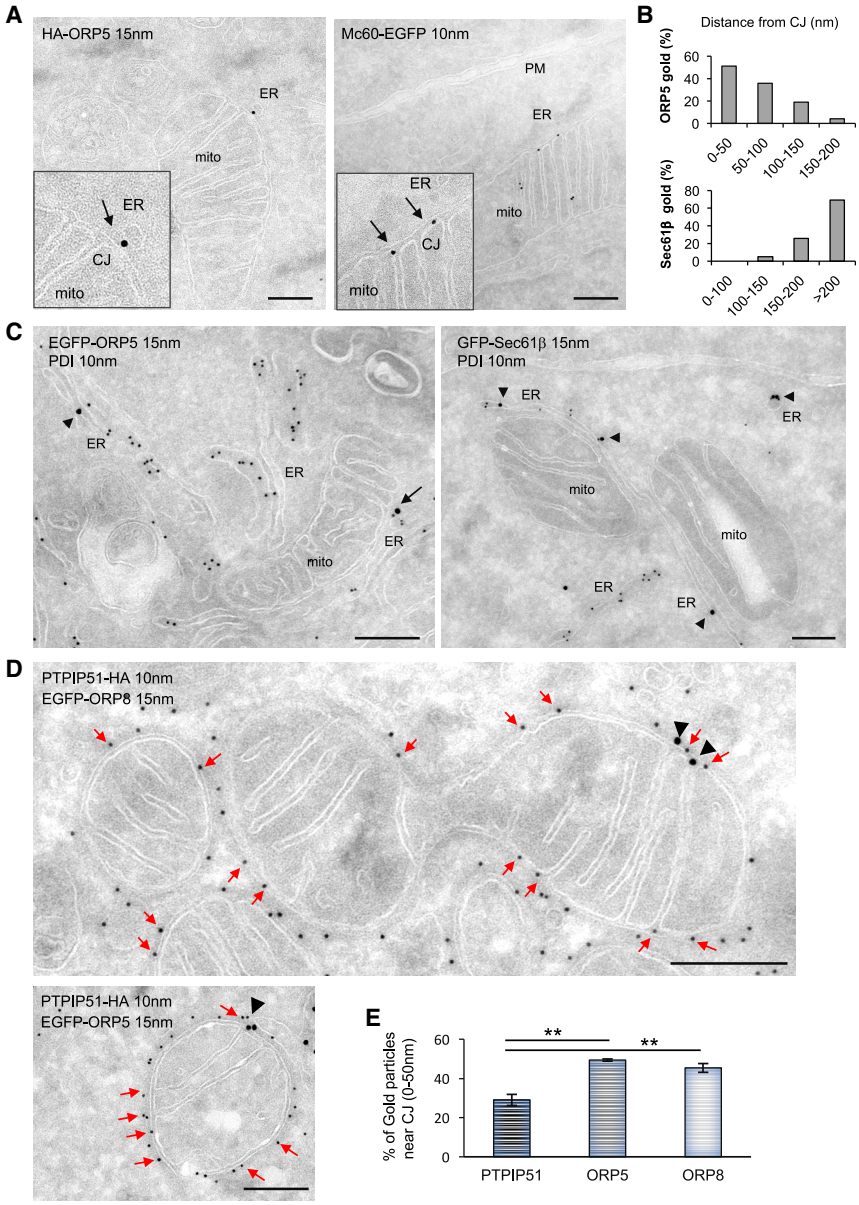

Figure 3. ORP5 localizes at ER-mitochondria contact sites near cristae junctions (CJs)

(A) Electron micrographs of ultrathin cryosections of HeLa cells transfected with HA-ORP5 or Mic60-EGFP and immunogold stained with anti-HA or anti-GFP (10 or 15 nm gold), showing ORP5 localization at ER-mitochondria contacts in close proximity to CJ (arrow) and the localization of the MICOS complex (Mic60) at CJ (arrows). Scale bar, 250 nm.

(B) Quantification of the proximity of HA-ORP5 and EGFP-Sec61b gold particles to the CJ. Results are presented as the percentage of ORP5 or Sec61b gold particles at specific ranges of distance (nm) from CJ. One-hundred and fifty gold particles were counted on randomly selected cell profiles in each sample.

(C) Electron micrographs of ultrathin cryosections of HeLa cells transfected with EGFP-ORP5 or GFP-Sec61b and immunogold labeled with anti-GFP (15 nm gold) and anti-PDI (10 nm gold). Note ORP5 localization at ER-mitochondria contacts near CJ (arrow) and Sec61b localization to ER membranes not in contact with the mitochondria membranes (arrowheads). Scale bar, 250 nm.

(D) Electron micrographs of ultrathin cryosections of HeLa cells transfected with EGFP-ORP8 or EGFP-ORP5 and PTPIP51-HA and immunogold labeled with anti-GFP (15 nm gold) and anti-HA (10 nm gold). Note ORP8 and ORP5 specific localization at ER-mitochondria contacts near CJ (black arrowheads) and PTPIP51 localization to all the mitochondria surface including CJ (red arrows). Scale bars, 250 nm.

(E) Quantification of PTPIP51-HA, EGFP-ORP8, and EGFP-ORP5 proximities to CJ. Results are presented as the percentage of gold particles within 0–50 nm from CJ ± SEM; 286 gold particles for PTPIP51 and 150 gold particles for ORP5 and ORP8 were counted on randomly selected cell profiles in each sample. Statistical analysis: unpaired Student's t test, $^{**}p < 0.01$.

although its score was lower than SAM50 and Mic60, and below the assigned threshold in the case of EGFP-ORP5 (50) (Figure 4A).

To confirm ORP5/8 interaction with SAM50 and Mic60, GFP pull-down experiments from HeLa cells expressing EGFP-ORP5, EGFP-ORP8, or EGFP alone were carried out (Figure 4B). Consistent with the MS data, endogenous SAM50 and Mic60 were recovered with both EGFP-ORP5 and EGFP-ORP8 but not with EGFP alone, confirming specific biochemical co-purification of ORP5 and ORP8 with SAM50 and Mic60.

Next, to determine the domains involved in the interaction of ORP5/8 with the MIB/MICOS complex, GFP pull down experiments were carried out from cells expressing EGFP-tagged ORP5 (EGFP-ORP5ΔPH) or ORP8 (EGFP-ORP8ΔPH) PH domain deleted constructs (Figures S4A and S4B), and compared with the full-length proteins (EGFP-ORP5 and EGFP-ORP8) or with the EGFP alone. In accord with the MS data, the deletion of the PH domain increased ORP5 and ORP8 interaction with SAM50, compared with the full-length proteins (Figure S4B). Confocal analysis of ORP5 and SAM50 localization in cells expressing EGFP-ORP5 or EGFP-ORP5ΔPH and stained with an anti-SAM50 antibody confirmed the stronger enrichment of the ORP5ΔPH construct at ER elements in contact with the SAM50-labeled mitochondria compared with the full-length ORP5 (Figure S4C).

As the PH domain is not required for the interaction with SAM50, we further investigated the role of the other domains of ORP5 in such interaction by immunoprecipitating ORP5 deletion mutants for the ORD or the TM domains (EGFP-ORP5-ΔORD, EGFP-ORP5ΔTM) (Figures S4A and S4B). While the

A

Mass-Spectrometry Analysis

		IP EGFP	IP EGFP-ORP5	IP EGFP-ORP5ΔPH
Protein	Localization	Mascot Score		
ORP5	MAMs	0	9689	12192
ORP8	MAMs	31	930	690
Mic60	IMM	43	579	1150
SAM50	OMM	0	237	516
metaxin 2	OMM	0	32	175
RHOT2	OMM	0	131	119
TOM22	OMM	0	77	95
PSS1	MAMs	0	150	200
PTPIP51	OMM	0	76	73

B

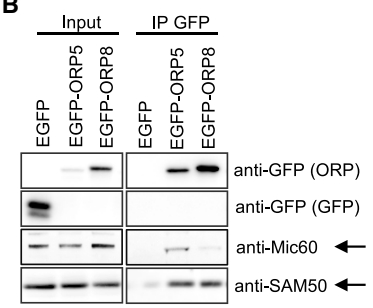

C

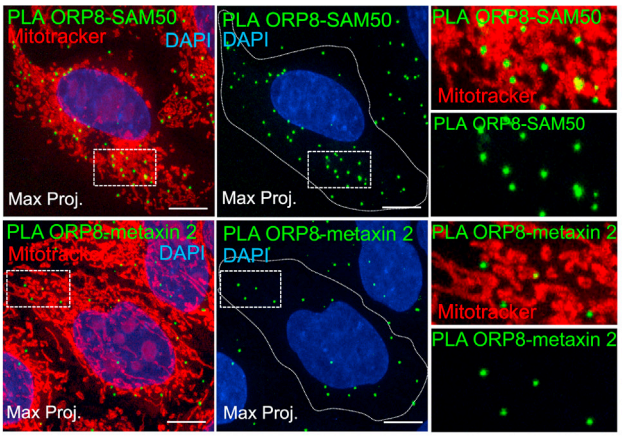

D

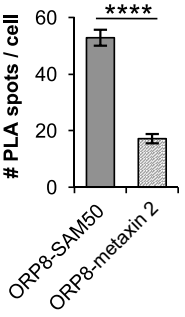

E

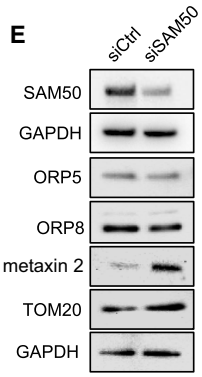

F

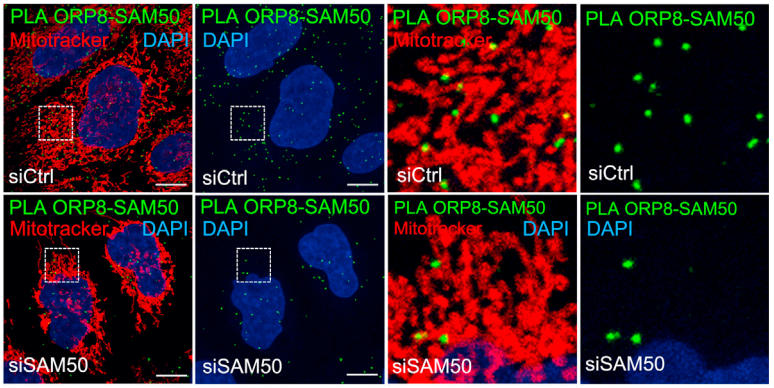

G

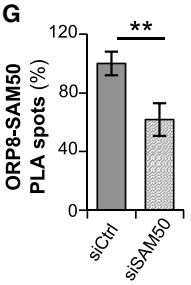

H

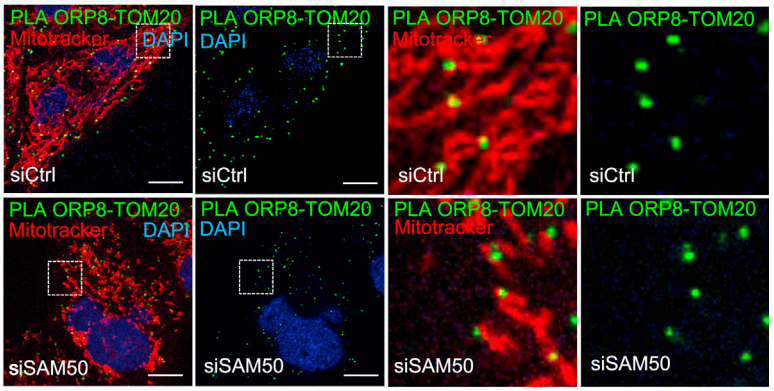

I

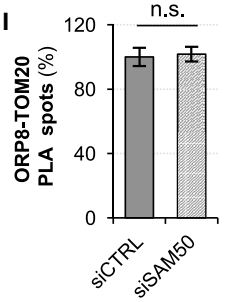

(legend on next page)

deletion of the ORD domain did not affect the interaction between ORP5 and SAM50, the deletion of the TM domain decreased the amount of SAM50 co-immunoprecipitated with ORP5, indicating that ORP5 should be properly anchored to the ER to localize at ER-mitochondria contact sites and to interact with SAM50 (Figure S4B).

To confirm the interaction between ORP5/8 and SAM50 at endogenous level we took advantage of the available antibodies against ORP8 and SAM50 from different species and analyzed their interaction using PLA (Duolink) by confocal imaging in HeLa cells. PLA signals corresponding to ORP8-SAM50 endogenous interaction were detected at ER-mitochondria contact sites in control cells (Figure 4C). Interestingly, PLA signals were also detected for ORP8-metaxin 2, although the number of spots was significantly minor (Figures 4C and 4D), correlating to the lower MS score of metaxin 2 (Figure 4A). Then, to further verify the specificity of ORP8-SAM50 PLA, we analyzed their interaction in cells where SAM50 was downregulated by RNAi (siSAM50) (Figures 4E and 4F). A decrease of about 40% of ORP8-SAM50 PLA was found in siSAM50 cells (Figures 4F and 4G), in accord with the decrease of the levels of SAM50 protein of about 40%–50% assessed by WB (Figure 4E), validating the specificity of the ORP8-SAM50 interaction. Similarly, the KD of SAM50 decreased the PLA interaction between ORP8 (and ORP5) and metaxin 2 (Figures S5A and S5D). To further investigate if this effect was specific for protein components of the MIB complex, we performed PLA interaction assays of ORP8 (and ORP5) with another OMM protein, TOM20, which is not a *bona fide* component of this complex. Interestingly, TOM20 also interacted with ORP8 and, to a minor extent, with ORP5, but these interactions were not decreased by the KD of SAM50 (Figures 4H and 4I and S5E and S5F). Also, these effects were not due to decreased levels of ORP5, ORP8, metaxin 2, and TOM20 proteins, as assessed by WB (Figure 4E).

To investigate a possible role of SAM50 and Mic60 in regulating the levels of ORP5/8 at MAMs, we analyzed their endogenous interaction by PLA and confocal microscopy in HeLa cells where either SAM50 or Mic60 were knocked down by small interfering RNA (siRNA). Interestingly, a significant decrease (of about 40%) in ORP5-ORP8 interaction in close proximity to mitochondria (corresponding to MAM) was found in both SAM50 and Mic60 KD cells, compared with control cells (Figures 5A and 5B), indicating a synergistic effect of SAM50/Mic60 on the ORP5-ORP8 interaction at MAM. Further localization analysis of endogenous ORP5 and ORP8 in siSAM50 cells confirmed decreased levels of these proteins at MAM (Figures 5C–5F). Together, our data reveal the specificity of the effects of SAM50 KD on ORP5 and ORP8 interaction with each other and with components of the MIB complex.

To verify the possibility of an indirect effect of SAM50 or Mic60 silencing on the morphology and abundance of MAMs, we carried out an ultrastructural analysis by conventional electron microscopy (EM) and horseradish peroxidase (HRP)-KDEL EM (carrying an HRP tagged with the ER retention motif of the [Lys-Asp-Glu-Leu] endoplasmic reticulum protein retention receptor 1 to stain the ER) in Mic60 or SAM50 silenced cells. Morphological analysis by conventional EM showed that transient KD of SAM50 or Mic60 induces formation of multilamellar cristae, almost devoid of CJs (Figures S6A and S6B), complementing previous observations by other groups through stable disruption of the MIB/MICOS functions (Ding et al., 2015; Ott et al., 2015). However, in both SAM50 and Mic60 KD cells, ER-mitochondria contact sites were still present and their morphology not altered (Figures 5G and S6A). Quantitative morphological analysis by HRP-KDEL EM in control and SAM50 or Mic60 silenced cells confirmed that the abundance of ER-mitochondria contact sites was not altered by SAM50 or Mic60 KD (Figure 5H), indicating that the effects on ORP5/8 interactions at MAMs were not indirect due to a global rearrangement of the ER-mitochondria contact sites.

Overall, our data reveal an interaction between ORP5/8 and the MIB/MICOS complex at ER subdomains associated with intra-mitochondrial membrane contacts facing CJ, and a direct

Figure 4. ORP5 and ORP8 interact with the MIB/MICOS complex at ER-mitochondria contacts

(A) Identification of mitochondrial proteins associated to mitochondrial outer or inner membranes (OMM, IMM) that interact with EGFP-tagged ORP5 constructs by mass spectrometry (MS). Note the presence of some proteins of the MIB complex: Mic60, SAM50, and metaxin 2 and of their interacting partner RHOT2. Interaction scores (Mascot scores) of Mic60, SAM50, and metaxin 2 with the EGFP-ORP5ΔPH construct are stronger than with EGFP-ORP5.

(B) Western blot analysis of ORP5, ORP8, SAM50, and Mic60 in immuno-precipitated samples obtained from lysates of HeLa cells transfected with EGFP-ORP5, EGFP-ORP8, or EGFP alone. ORP5 and ORP8 were detected using antibodies against GFP.

(C) Representative confocal images showing endogenous ORP8-SAM50 and ORP8-metaxin 2 PLA interactions (green), mitochondrial network (MitoTracker, red), and nuclei (DAPI, blue) in HeLa cells. Images are displayed as maximum projection of all layers. Scale bar, 10 μm.

(D) Quantitative analysis of endogenous ORP8-SAM50 and ORP8-metaxin 2 PLA interactions in HeLa cells. Data are shown as mean values ± SEM of n = 36 cells, ORP8-SAM50; n = 39 cells, ORP8-metaxin 2. Statistical analysis was performed using unpaired Student's t test; ****$p < 0.0001$.

(E) Western blot analysis of ORP5, ORP8, SAM50, TOM20, and metaxin 2 in protein lysates obtained from HeLa cells treated with scrambled siRNA (siCtrl) and from HeLa cells treated with siRNA targeting SAM50 (siSAM50).

(F) Confocal images of control (siCtrl) and SAM50 (siSAM50) knockdown HeLa cells showing endogenous interaction of ORP8-SAM50 by Duolink PLA (green) at MAMs. Mitochondria are labeled by MitoTracker (red) and nuclei by DAPI (blue). Images are presented as maximum projection of all layers. Insets show magnifications of the boxed regions. Scale bar, 10 μm.

(G) Quantification of endogenous ORP8-SAM50 PLA signals in control and SAM50 knockdown HeLa cells, showing the reduction of about 50% of ORP8-SAM50 PLA in SAM50 knockdown cells compared with control. Bars indicate mean values ± SEM. Number of cell analyzed: siCtrl (n = 30), siSAM50 (n = 22). Statistical analysis: p values were determined by unpaired Student's t test; **$p < 0.01$.

(H) Representative confocal images showing endogenous ORP8-TOM20 PLA interactions (green), mitochondria (MitoTracker, red), and nuclei (DAPI, blue) in control and SAM50 knockdown HeLa cells. Images are displayed as single layers. Scale bar, 10 μm.

(I) Quantitative analysis of endogenous ORP8-TOM20 PLA interactions in HeLa cells. Data are shown as mean values ± SEM of n = 49 cells, siCtrl; n = 49 cells, siSAM50; n.s., not significant.

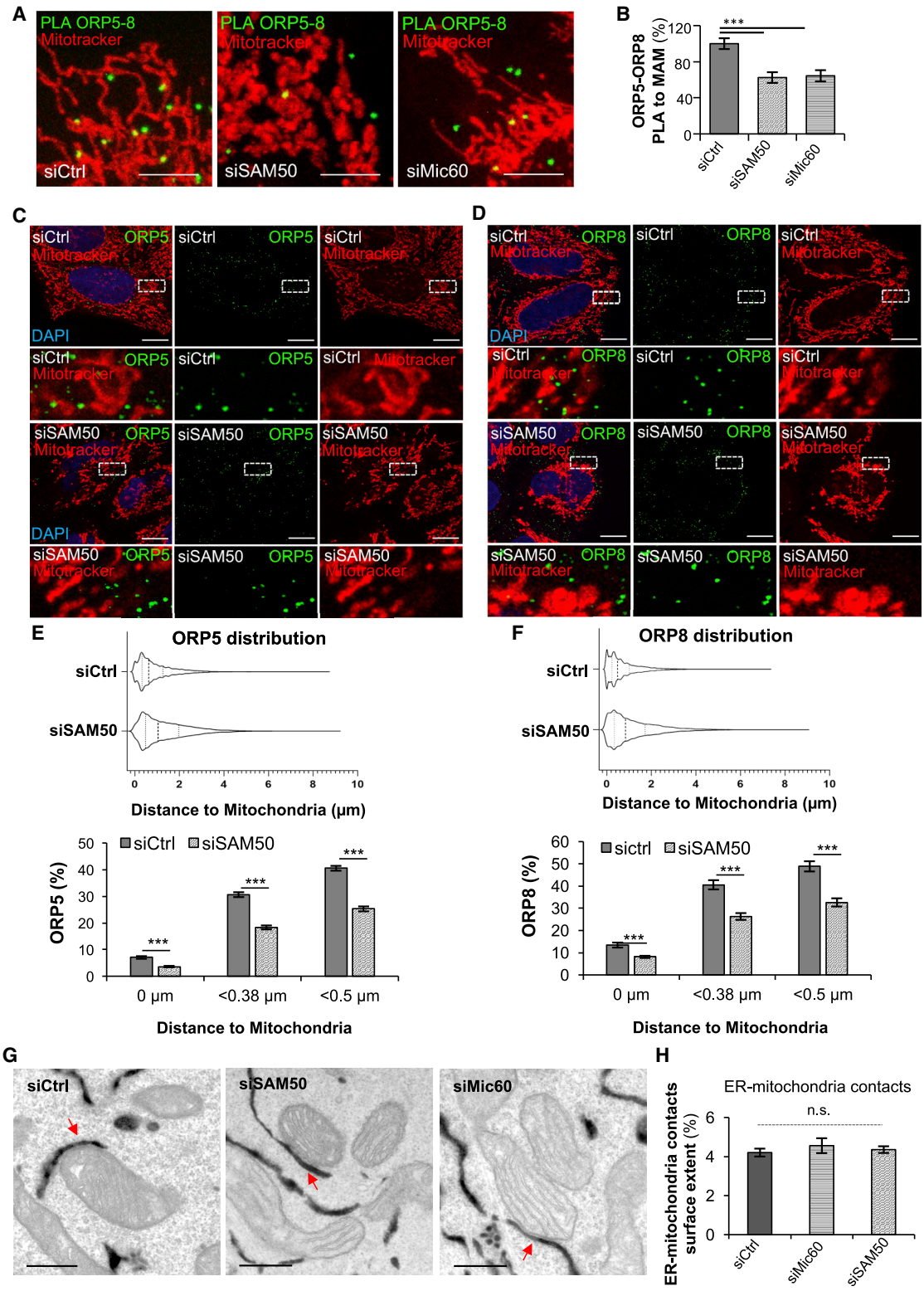

Figure 5. SAM50 and Mic60 knockdowns induce a decrease in ORP5-ORP8 interaction at MAMs but do not alter the abundance of ER-mitochondria contact sites

(A) Confocal images of a region of Ctrl (siCtrl), SAM50 (siSAM50), and Mic60 (siMic60) knockdown HeLa cells showing endogenous interaction of ORP5 and ORP8 by Duolink PLA (green) near mitochondria (MitoTracker, red). Scale bar, 5 μm.

(legend continued on next page)

role of the MIB/MICOS complex in ORP5/8 targeting/interactions at MAMs.

ORP5/ORP8 and the MIB/MICOS complex regulate PS-to-PE conversion at the ER-mitochondria interface

The role of ORP5 and ORP8 in lipid transport at ER-mitochondria contacts still remains to be established. We tested whether ORP5 and ORP8 could mediate PS transport at the ER-mitochondria interface by measuring levels of mitochondrial PE in the mitochondrial fraction isolated from HeLa cells (as in Galmes et al., 2016) where ORP5 or ORP8 were transiently silenced by RNAi. As the ER-derived PS is the major precursor for mitochondrial PE, if ORP5 and ORP8 mediate non-vesicular transport of PS from the ER to the mitochondria, their absence should lead to a reduction of mitochondrial PE. We chose to use a transient KD as it overcomes the limits and/or compensatory effects on lipid transport/biosynthetic pathways that other stable approaches could induce. The purity of mitochondria and of the other subcellular fractions was verified in control, ORP5, and ORP8 KD conditions by WB by probing the samples for cytochrome *c* as mitochondrial marker and IP3R-3 as a MAM-enriched marker (Figure 6A). All markers were highly enriched in their respective fractions and were absent in the others, and, as previously shown (Galmes et al., 2016), ORP5 and ORP8 were enriched in the MAM fraction and absent in the mitochondria fraction of control cells (Figure 6A). On the contrary, they were strongly suppressed in ORP5 and ORP8 KD cell lysates and in the respective MAM fractions (Figure 6A). MS-lipidomic analysis revealed a specific reduction of PE levels in mitochondria isolated from ORP5 and ORP8 KD cells, of 34% and 20%, respectively, compared with control cells (Figure 6B), while PE levels from total cells were unchanged. Additionally, the mitochondrial levels of two other phospholipids (PI and PC) were not perturbed by ORP5/8 depletion (Figure S8A). The decrease in PE could be due to a decrease in the protein levels of the PS-decarboxylase (PISD) or the PS-synthase 1 (PSS1) enzymes mediating PS-to-PE conversion on mitochondria and PS synthesis in the ER, respectively. To exclude this possibility, we analyzed the protein levels of PISD and PSS1 by WB in ORP5, ORP8, or ORP5 + ORP8 KD cells and compared them with control cells (Figure S8B). We found no significant difference but rather a slight increase in the enzymes upon ORP5 and/or ORP8 KDs. These data suggest that ORP5 and ORP8 could transfer PS at ER-mitochondria contact sites.

The ORD domain of ORP8 (ORD8) has been shown to transfer PS between liposome membranes in counter-transport with PI4P or PIP_2 *in vitro* (Chung et al., 2015; Ghai et al., 2017). However, the lipid transfer activity of ORP5 ORD domain (ORD5) has not been studied so far. Also, the ability of ORD5 and ORD8 to transfer PS independently of a gradient of PI4P or PIP_2 or other phospholipids than PS has never been addressed. Thus, we purified the recombinant ORD5 and ORD8 from bacteria (Figure S7A) and compared their ability to transport fluorescent phospholipids (TopFluor-PS, -PC, or -PE) from donor to acceptor liposomes *in vitro*. Donor liposomes containing fluorescent phospholipids and biotinylated lipids were first immobilized on streptavidin beads and then mixed with acceptor liposomes in the presence or absence of ORP5/8 ORD domains (Figure S7B). After 1 h at 37°C, acceptor liposomes were recovered from the supernatant and their fluorescence was measured (Figure S7B). Our results show that both ORD5 and ORD8 transfer PS, but not PC and PE, from donor to acceptor liposomes (Figure S7C). They also reveal that ORD5 and ORD8 share equivalent ability to transfer PS *in vitro*. To confirm that fluorescent lipids were indeed transferred to the acceptor liposomes, a fraction of the reaction supernatant was floated on a Nycodenz density gradient by ultracentrifugation and the fluorescence in the top fraction of the gradient (containing floated acceptor liposomes) was measured (Figure S7D). Fluorescence of TopFluor-PS in the acceptor liposomes was maintained after their floatation, confirming its effective transfer between liposomes *in vitro*.

In subsequent experiments, we measured the levels of mitochondrial PE newly synthesized from the ER-derived PS by using a radiometric PS-to-PE conversion assay *in situ* (Shiao et al., 1995) in ORP5, ORP8, or ORP5 + 8 silenced or control HeLa cells (Figure 6C). This assay allows the monitoring of PS transfer from the ER to mitochondria by measuring the levels of radioactive PS and PS-derived PE by thin-layer chromatography (TLC) after incorporation of radioactive L-[^{3}H(G)]-serine into the cells. A significant decrease in the levels of newly synthetized PE was found in ORP5 and in ORP5 + ORP8 KD cells (Figure 6C). The decrease was stronger in ORP5 + ORP8 KD cells, indicating a cooperative

(B) Quantification of ORP5-ORP8 PLA signals in control, SAM50 and Mic60 knockdown HeLa cells, showing the decrease of about 40% of ORP5-ORP8 PLA in SAM50 and Mic60 knockdown cells compared with control. Bars indicate mean values ± SEM. Number of cell analyzed: siCtrl (n = 33), siSAM50 (n = 19), siMic60 (n = 24). Statistical analysis: unpaired Student's t test, ***p < 0.001.

(C and D) Confocal images showing endogenous ORP5 (green) and ORP8 (green) localization in relation to mitochondria (MitoTracker, red) in Ctrl (siCtrl) and SAM50 (siSAM50) knockdown HeLa cells. Nuclei are stained with DAPI (blue). Images are represented as single layers. Magnifications of white boxed regions are shown for each condition. Scale bar, 10 μm.

(E and F) Quantitative analysis of ORP5 and ORP8 distribution in relation to their distance to mitochondria in HeLa cells treated with scrambled siRNA (siCtrl) and siRNA targeting SAM50 (siSAM50). Violin plots display overall frequency and distribution of ORP5 and ORP8 labeling in relation to their distance to mitochondria. Median values (wider dotted line) anti-ORP5, siCtrl = 0.61 μm, siSAM50 = 1.04 μm; anti-ORP8, siCtrl = 0.48 μm, siSAM50 = 0.84 μm. Interquartile range (narrow dotted lines) anti-ORP5, siCtrl 25% and 75% percentile = 0.32 and 1.26 μm, siSAM50 25% and 75% percentile = 0.48 and 1.97 μm; anti-ORP8, siCtrl 25% and 75% percentile = 0.23 and 1.01 μm, siSAM50 25% and 75% percentile = 0.34 μm and 1.7 μm. Column charts display the percentage of ORP5 and ORP8 labeling whose distance from mitochondria is 0 μm, <0.38 μm, and <0.5 μm. Data are expressed as mean values ± SEM. Number of cell analyzed: anti-ORP5, siCtrl n = 37, siSAM50 n = 40; anti-ORP8, siCtrl n = 22, siSAM50 n = 29. Statistical analysis: p values were determined by unpaired Student's t test, ***p < 0.001.

(G) Representative electron micrographs of HeLa cells treated with Ctrl siRNAs or siRNAs against SAM50 or Mic60 and transfected with HRP-KDEL. Red arrows indicate ER-mitochondria contact sites. Scale bar, 500 nm.

(H) Quantifications of the extent of ER-mitochondria contact sites in Ctrl, Mic60, and SAM50 knockdown cells expressing HRP-KDEL. Data are shown as percentage of the ER in contact with mitochondria (mitochondria occupancy) ± SEM, n = 30 for siCtrl, n = 20 cell profiles for siMic60 and siSAM50 and 1,000 mitochondria; n.s., not significant.

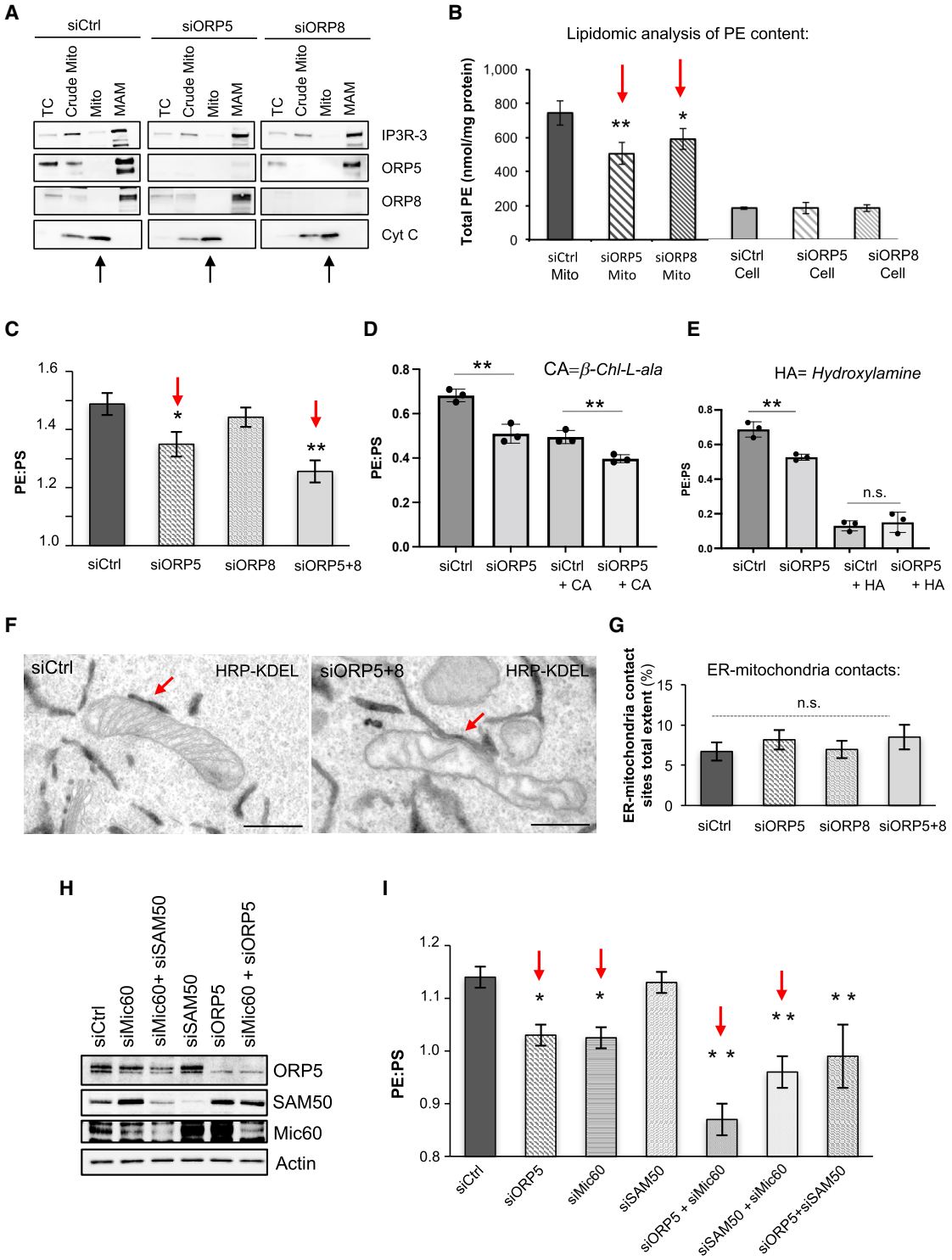

Figure 6. ORP5/8 and the MIB/MICOS complex regulate levels of PS-derived mitochondrial PE

(A) Crude mitochondria, mitochondria, and MAM fractions were purified from Ctrl, ORP5, and ORP8 siRNA-treated HeLa cells. Equal amounts of protein from each fraction were loaded on a 4%–20% gradient SDS-PAGE gel and immunoblotted using anti-ORP5, anti-ORP8, anti-IP3R-3 (MAM protein), and anti-cytochrome *c* (mitochondrial protein). Mito, mitochondria; MAM, mitochondria-associated ER membrane.

(B) MS-based quantification of the PE content (nmol/mg protein) of mitochondria isolated from Ctrl, ORP5, or ORP8 knockdown cells and of Ctrl, ORP5, or ORP8 knockdown intact cells. Data are shown as mean of three independent replicates ± SEM. Statistical analysis: unpaired Student's t test, *p < 0.05, **p < 0.01.

(legend continued on next page)

effect of ORP5 and ORP8 in this process. A slight, not statistically significant decrease was also found in ORP8 KD cells, suggesting a major role of ORP5 compared with ORP8 in PS transfer at ER-mitochondria contact sites *in situ*. As [^{3}H]-serine radioactivity could be incorporated to PE also via an alternative pathway involving sphingosine (Hanada et al., 1992), we next sought to address the contribution of this pathway to PE labeling, by repeating the experiments in control and ORP5 KD cells in the presence (throughout pulse and chase of [3H]-serine) of β-chloro-L-alanine, an inhibitor of serine palmitoyltransferase (Chen et al., 1993). Although a decrease in newly synthesized PE was observed in siCtrl cells upon addition of β-chloro-L-alanine, PS-to-PE conversion was significantly reduced in β-chloro-L-alanine treated and untreated ORP5 knockdown cells (∼17% and ∼23% respectively), compared with control (Figure 6D). We then verified that the fraction of PE decreasing upon ORP5 KD was indeed derived from conversion of PS by PISD by measuring PS-to-PE conversion in the presence of hydroxylamine, an inhibitor of PISD activity (Figure 6E). Treatment with 5 mM hydroxylamine robustly inhibited PS-to-PE conversion in both control and ORP5 KD cells, the level of residual conversion being similar in both of these cells, further confirming that the reduction in mitochondrial PE induced by depletion of ORP5 is essentially due to the decrease in PS transfer from the ER to the mitochondria (Figure S8E). The β-chloro-L-alanine and hydroxylamine data also suggest that at least 80% of the serine labeling of PE occurs via the PS decarboxylase reaction in HeLa cells, in accord with a previous work in another cell type, the baby hamster kidney fibroblasts (BHK cells), showing that only certain minor PE species are labeled from the sphingosine-PE pathway (Heikinheimo and Somerharju, 1998).

To test whether the effects on PS transport at ER-mitochondria contacts were specific for ORP5 and ORP8 loss of function or simply due to a decrease of ER-mitochondria contacts induced by their KD, we quantified the abundance of ER-mitochondria contact sites by EM in control and ORP5, ORP8, or ORP5 + ORP8 KD cells. To facilitate the visualization of the ER we transfected the cells with a HRP-KDEL construct that stains the ER with a dark signal. Our quantifications revealed that ORP5, ORP8, or ORP5 + ORP8 KDs did not affect the extent of ER-mitochondria contacts (Figures 6F and 6G). The total mitochondrial mass (quantified as mitochondrial surface/cell) was also unchanged (Figure S8C). These results indicate that ORP5 and ORP8 act as LTPs rather than tethers (Figures 7 and S8E).

Even a modest reduction (22%–27%) of mitochondrial PE levels in mammalian cells has been shown to profoundly alter the morphology of mitochondrial cristae as well as mitochondria functions (Tasseva et al., 2013). Accordingly, 52% of mitochondria in ORP5 + ORP8 double-KD cells display aberrant cristae morphology versus 9% in control cells (Figures 6F and S8D). These defects in cristae morphology were also observed by conventional EM (Figure S6A) and were similar to those previously shown in the case of ORP5 and ORP8 individual KD (Galmes et al., 2016). Interestingly, the percentage of mitochondria with altered morphology in ORP5 + ORP8 double-KD cells was higher compared with ORP8 KD (Galmes et al., 2016), reflecting the stronger effect of ORP5 + ORP8 double KD on PS transport at ER-mitochondria contact sites (Figures 6C and S8D).

Decreased levels of PE strongly affect the organization of the mitochondrial respiratory supercomplexes (Tasseva et al., 2013). We had previously shown that ORP5 KD induces a reduction in the basal mitochondrial oxygen consumption rate (OCR_{BAS}), indicative of reduced respiratory activity (Galmes et al., 2016). However, it remains questioned whether ORP8 could also reduce OCR_{BAS} and if this reduction could be exacerbated under metabolic stress conditions. Thus, we monitored mitochondrial oxygen consumption rate (OCR) in control, ORP5, or ORP8 KD cells in basal and in stress conditions (Figure S9). ORP5 KD induced a significant reduction in both OCR_{BAS} (∼37%) and OCR upon FCCP treatment (OCR_{FCCP}) (∼36%). Interestingly, ORP8 KD also induced a significant decrease in OCR_{BAS} (∼31%) and OCR_{FCCP} (∼29%), although the decreases were less prominent than upon ORP5 KD. These data uncover a key role of ORP5 and ORP8 in preserving mitochondrial respiratory activity in basal and in stress conditions, and a major impact of ORP5 in this process, in accord with its major role in PS transfer at ER-mitochondria contact sites.

To test whether the interaction of ORP5 with the MIB complex could facilitate the non-vesicular transfer of PS from the ER to the mitochondrial membranes (and consequently synthesis of mitochondrial PE), we performed radiometric PS-to-PE conversion

(C) HeLa cells transfected with siCtrl, siORP5, siORP8, or siORP5+ORP8 RNAi oligos were incubated with L-[^{3}H(G)]serine (30.9 Ci/mmol) for 18 h. After extraction and separation of lipids by TLC, PS and PE spots were scraped and analyzed for [^{3}H] radioactivity, as described in STAR Methods. Each condition was analyzed in triplicate in each of three independent biological replicates. Data are presented as mean of PE:PS ratio ± SEM. Statistical analysis: unpaired Student's t test, *$p < 0.05$, **$p < 0.01$ compared with Ctrl.

(D) Cells transfected with siCtrl and siORP5 oligos were treated with 1 mM β-chloro-L-alanine (CA, β-Chl-L-ala, inhibitor of Ser-palmitoyltransferase) or untreated, then pulsed with 7 μCi/mL of [3H(G)]serine for 1 h and chased for 4 h in serum-free DMEM + β-chloro-L-alanine, before analysis. n.s., not significant; **$p < 0.01$ compared with Ctrl.

(E) Similar experiments were performed in presence of 5 mM hydroxylamine (HA, inhibitor of PS decarboxylase). n.s., not significant, **$p < 0.01$ compared with Ctrl.

(F) Electron micrographs of HRP-KDEL-expressing HeLa cells treated with Ctrl siRNAs (siCtrl) or siRNAs against ORP5 and ORP8 (siORP5 + siORP8). Red arrows indicate ER-mitochondria contact sites. Scale bar, 500 nm.

(G) Quantifications of the total extent of ER-mitochondria contact sites in siCtrl, siORP5, siORP8, and siORP5 +8 cells expressing HRP-KDEL. Data are shown as percentage of the ER surface length in contact with mitochondria ± SEM, n = 20 cell profiles and ±900 mitochondria; n.s., not significant.

(H) Western analysis showing ORP5, SAM50, Mic60, and actin levels in protein lysates from HeLa cells treated with siRNA against Ctrl, ORP5, Mic60, or SAM50. Arrow indicates the specific band for Mic60.

(I) Radiometric measurement of PS-to-PE conversion in the indicated siRNAs. Data are presented as mean of PE:PS ratio ± SEM. Each condition was performed in triplicate in each of the independent biological replicates (n = 5 for siCtrl and siORP5; n = 4 for siSAM50; n = 3 for the other siRNAs conditions). Statistical analysis: unpaired Student's t test, *$p < 0.05$, **$p < 0.01$ compared with Ctrl.

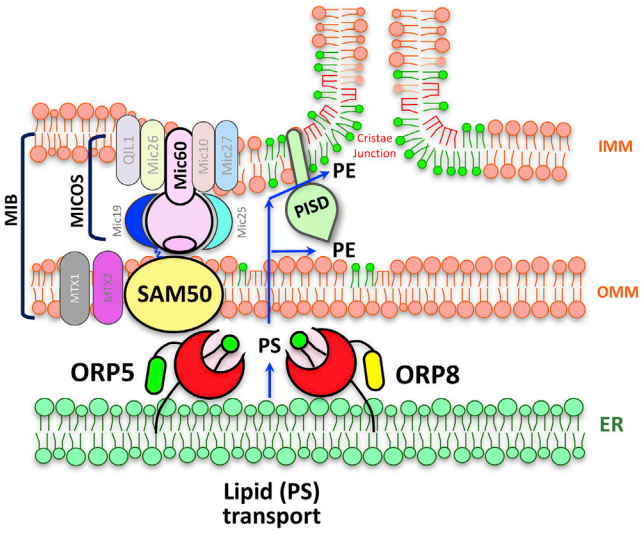

Figure 7. PS transport at ER-mitochondria contact site subdomains associated to MIB/MICOS complex

ORP5/8 mediate the transfer of PS from ER to mitochondria at ER-mitochondria membrane contact sites. This transfer occurs at ER subdomains facing the CJs where ORP5/8 interacts with SAM50 and Mic60, key proteins of the MIB/MICOS complex (some of the other MIB/MICOS components are included in this simplified cartoon). This interaction facilitates the transfer of PS from ER to the mitochondrial membranes at the level of CJ and PS conversion into PE, a phospholipid that plays a critical role in cristae organization and mitochondrial function.

assay in cells depleted of ORP5, SAM50, or Mic60 alone or in combination by RNAi. Robust KD of ORP5, SAM50, or Mic60 was confirmed by WB after 48 h (Figure 6H). Analysis of PS-derived newly synthetized PE revealed a significant decrease in PE in ORP5 and Mic60 KD cells (Figure 6I). Moreover, the double KD of ORP5 and Mic60 had an additive effect, supporting a cooperation of these two proteins in the regulation of PE synthesis. However, the levels of PE were not changed in SAM50 KD cells compared with control. This could be explained by the fact that other subunits of the MIB complex might compensate for its depletion. Indeed, protein levels of Mic60 and metaxin 2 were strongly increased upon SAM50 KD (Figures 4E and 6H). Interestingly, the double silencing of SAM50 and either ORP5 or Mic60 had a significant impact on PE synthesis that was even stronger compared with the individual KDs (Figure 6I).

EM analysis of mitochondria morphology in all KD conditions revealed that downregulation of ORP5, SAM50, or Mic60, individually or in combination, induced formation of multilamellar cristae, almost devoid of CJs (Figures S6A and S6B). However, in all KD conditions, ER-mitochondria contact sites were still present and their morphology was not altered (Figures 5G and 5H and S6A), indicating that the effects on PS-derived PE synthesis were specifically due to ORP5, Mic60, or SAM50 loss of function effects on PS transport at ER-mitochondria contacts or on the maintenance of intra-mitochondrial membrane bridges, respectively.

Overall, our results reveal that ORP5/8 cooperate with the MIB/MICOS complex to regulate the transfer of PS from the ER to the mitochondrial membranes necessary for synthesis of mitochondrial PE and consequently for maintaining mitochondrial cristae morphology and respiration (Figure 7).

DISCUSSION

In this study, by using a combination of biochemical and imaging approaches, we uncover the endogenous localization of ORP5 and ORP8, revealing that they are mainly localized at ER-mitochondria contact sites and providing the evidence for a physiological relevance of the ORP5/8 complex at MAMs (Figures 1 and 2 and S1–S3). So far, ORP5 and ORP8 localization have been only studied in conditions where one of these two partner proteins was expressed in high excess compared with the other one. Previous studies, including one from our group, have shown that overexpression of ORP5 induces an increase of ER-PM contacts where the protein also localizes (Chung et al., 2015; Galmes et al., 2016). Consequently, several following studies have addressed the role of ORP5 and ORP8 at ER-PM contacts, overlooking their function at MAM. However, the increase in cortical ER observed upon ORP5 overexpression does not reflect the physiological abundance of ER-PM contacts, as the cortical ER in non-specialized cells generally covers not more than 5% of the plasma membrane surface. Indeed, we have found that the increased localization of ORP5 to cortical ER when overexpressed alone does not reflect its endogenous localization when it is in complex with ORP8, which is instead enriched at MAMs. Our findings have important implications for a better understanding of the physiological localization and function of ORP proteins but also of other proteins that assemble in multimeric complexes at ER-mediated membrane contact sites, such as the E-Syts (Giordano et al., 2013).

Our study reveals that ORP5/8 physically interact with SAM50 and Mic60, two key components of the MIB/MICOS complex that anchor the IMM to the OMM at the level of CJ (Huynen et al., 2016; Ott et al., 2015; Wollweber et al., 2017). The biochemical interaction between ORP5 and SAM50/Mic60 uncovers the existence of a physical link between ER-mitochondria contact sites involved in lipid transport and intra-mitochondrial membrane contacts. ORP5 localization by IEM at ER-mitochondria contact sites near the CJ, where Mic60 and MICOS complex also reside, further confirms the existence of such tripartite membrane contact site structure. Moreover, KD of SAM50 and Mic60 does not affect ER-mitochondria contact sites, but specifically perturbs ORP5 and ORP8 interactions with each other and with metaxin 2, another component of the MIB complex at MAMs.

Importantly, here we describe a new function of ORP5 and ORP8 in the maintenance of mitochondrial levels of PE, an essential phospholipid of mitochondria, providing evidence of mammalian LTPs directly mediating non-vesicular transfer of PS (lipid precursor of mitochondrial PE) from the MAMs to the mitochondria at ER-mitochondria contact sites.

Other LTPs have recently been identified at ER-mitochondria contact sites in mammalian cells. Hirabayashi et al. (2017) recently showed that the SMP-containing protein PDZD8 is involved in ER-mitochondria tethering and in the regulation of Ca^{2+} dynamics in mammalian neurons. Although PDZD8 is a

structural and functional paralog of the Mmm1 subunit of the ERMES complex (Wideman et al., 2018), its function in lipid transport at ER-mitochondria contact sites remains unclear. Recently, the mammalian LTP VPS13A has been shown to localize to contact sites, including ER-mitochondria contacts (Kumar et al., 2018). VPS13A contains a lipid-binding domain (VPS13α) that has the ability to harbor multiple phospholipids at once and transfer them between liposomes *in vitro*. However, its role in lipid transfer at ER-mitochondria membrane contact sites *in situ* has not yet been established. Differently from the SMP and VPS13α domains that can simultaneously host multiple phospholipids, the ORD domain of Osh/ORPs forms a cavity that can host only one lipid at a time, thus improving specificity (Maeda et al., 2013; Wang et al., 2019).

An important finding of our work is that ORP5 and ORP8 KD do not affect the extent of ER-mitochondria contact sites, revealing that the main function of ORP5/8 at MAMs is lipid transfer and not membrane tethering. This is a unique feature among the LTPs that have been identified so far at MAMs. For instance, KD of PDZD8 and VPS13A result in a decrease of ER-mitochondria contact sites (Hirabayashi et al., 2017; Kornmann et al., 2009; Kumar et al., 2018), making it difficult to dissect the lipid transfer activity from the tethering function of these LTPs. Thus, ORP5/8 represent a so-far unique example of LTPs that specifically mediate lipid transport at ER-mitochondria contact sites, independently of membrane tethering, and that can thus be used as tools to specifically study lipid transport at MAMs.

ORP5 and ORP8 have previously been shown to counter-exchange PS with the PM phosphoinositides PI4P and PIP_2 at ER-PM contact sites in HeLa cells (Chung et al., 2015; Ghai et al., 2017). However, PI4P and PIP_2 are not present on the mitochondrial membranes, while PE is highly abundant in these membranes, in addition to being an essential lipid of all biological membranes. Our *in vitro* data show that the ORD domains of ORP5 and ORP8 transport PS, but not other phospholipids such as PE and PC, indicating a specific role of ORP5/8 in PS transport and excluding the possibility that ORP5/8 might also participate in the transport of a fraction of PE back to the ER. It is possible that ORP5/8 cooperate with other LTPs, such as VPS13A, for the exchange of other lipids (including PE) at ER-mitochondria contact sites. Importantly, we have confirmed the role of ORP5/8 in PS transfer by measuring a specific decrease of PS-derived mitochondrial PE in ORP5-depleted HeLa cells *in situ* (and even more upon ORP5 + 8 silencing) as well as a reduction of total PE in mitochondria isolated from these cells (Figures 6A–6E and S8A and S8B). Accordingly, ORP5/8 KD affects cristae morphology and the respiratory function of mitochondria (Galmes et al., 2016) (Figures 6F and 6G and S6 and S8D), all phenotypes that are expected in the case of even a mild decrease in mitochondrial PE (Joshi et al., 2012; Steenbergen et al., 2005); (Tasseva et al., 2013). Our data also suggest that the gradient of PS at ER-mitochondria contacts is sufficient to trigger the ORP5/8-mediated transport of PS from the MAMs, where it is highly enriched, to the mitochondria membranes, where it is rapidly converted into PE and is therefore present at a very low concentration. Our findings have important implications in the general field of LTPs, as they suggest that the same LTP can use different means to transfer lipids depending on the local gradients present at the specific membrane contact sites where it is localized.

Importantly, we also show that the *de novo* synthesis of mitochondrial PE requires both ORP5/8 at ER-mitochondria contact sites and the MIB/MICOS complex at intra-mitochondrial OMM-IMM contact sites (Figure 6I). Interestingly, recent evidence in yeast suggests that, in addition to the classical PE synthesis at the IMM by the IMM-localized PS-decarboxylase PISD, PE can also be synthesized in *trans* on the OMM (Aaltonen et al., 2016). Thus, it is possible that this alternative pathway, which requires MIB/MICOS tethering function to bring the mitochondrial intermembrane domain of PISD close to the OMM for synthesis of PE, is also conserved in mammalian cells. The cooperation of ORP5 (through its lipid transfer activity at ER-mitochondria contact sites) with SAM50 and Mic60 (through their OMM-IMM tethering function) could facilitate the movement of PS from the ER to the IMM, where it is converted to PE through the classical PE synthesis pathway, or through PISD function in *trans* on the OMM. Taken together these findings provide evidence of a physical and functional link between ER-mitochondria contacts and intra-mitochondrial membrane contacts maintained by the MIB/MICOS complexes, to facilitate transport of PS from the ER to the mitochondria and PE synthesis on the mitochondrial membranes (Figure 7).

In conclusion, our data reveal that (1) ORP5 and ORP8 form a protein complex that is endogenously enriched at ER-mitochondria contacts; (2) ORP5/8 constitute a molecular machinery that mediates PS transfer at ER-mitochondria contact sites but not ER-mitochondria tethering; and (3) ER-mitochondria contacts where ORP5/8 localize are physically associated with intra-mitochondrial contacts, maintained by the MIB/MICOS complex, to facilitate the transport of PS from the ER to mitochondria membranes. Overall our study provides a first molecular clue on how lipids are transported at ER-mitochondria contact sites and a functional insight into the complex interplay of the ER with the mitochondria and the intra-mitochondrial membrane contacts and associated machinery.

Limitations of the study

Because of their very low expression levels in cells, it was not possible to analyze endogenous ORP5/8 and SAM50/Mic60 co-localization by high-resolution immuno-EM. Moreover, although we have shown physical interaction of endogenous ORP5/8 and SAM50 at ER-mitochondria contacts by PLA, we cannot exclude that ORP5/8 and SAM50/Mic60 interact indirectly and are part of a larger functional complex in conjunction with other tethers or LTPs at contact sites. We also cannot exclude the possibility that, beyond ORP5/8, other LTPs and/or tethers contribute to regulate PS transport either as separate entities or in partnership with ORP5/8-MIB/MICOS complex. A possible partner is the mitochondrial protein MIGA2, recently shown to transport phospholipids, with a preference for PS, at ER-mitochondria contacts (Kim et al., 2022).

STAR★METHODS

Detailed methods are provided in the online version of this paper and include the following:

- KEY RESOURCES TABLE
- RESOURCE AVAILABILITY
  - Lead contact
  - Materials availability
  - Data and code availability
- EXPERIMENTAL MODEL AND SUBJECT DETAILS
  - Cell line
- METHOD DETAILS
  - cDNA plasmids and molecular cloning
  - Cell transfection
  - RNA interference
  - mRNA analyses by quantitative reverse transcriptase PCR (qPCR)
  - Immunoprecipitation of ORPs
  - Western blotting
  - Mass spectrometry-proteomic analysis
  - Cell fractionation
  - Mass spectrometry-lipidomic analysis
  - Immunofluorescence
  - *In situ* proximity ligation assay (PLA)
  - Electron microscopy analysis
  - ORP5 and ORP8 ORD domain purification
  - Liposome preparation
  - Lipid transfer assay *in vitro*
  - Radiometric assay for the conversion of PS to PE *in situ*
  - Mitochondrial respiration assay
- QUANTIFICATIONS AND STATISTICAL ANALYSIS

SUPPLEMENTAL INFORMATION

Supplemental information can be found online at https://doi.org/10.1016/j.celrep.2022.111364.

ACKNOWLEDGMENTS

We thank Dr V. Kozjak-Pavlovic and P. Somerharju for kindly sharing reagents and advice with us. We also thank Dr. R. Legouis and Dr. Emmanuel Culetto for discussion and for critically reading the manuscript; Claire Boulogne, Sandrine Lécart, and Remi Le Borgne for help and consultation with microscopy experiments; and Valentin Guyard, Blandine Bourigault, Riikka Kosonen, and Liisa Arala for technical assistance. The present work has benefited from the Imagerie-Gif core facility supported by l'Aslgence Nationale de la Recherche (ANR-11-EQPX-0029/Morphoscope, ANR-10-INBS-04/FranceBioImaging; ANR-11-IDEX-0003-02/Saclay Plant Sciences). For the Immuno-EM and HRP-KDEL EM analysis/quantifications we acknowledge the ImagoSeine facility, a member of the France BioImaging infrastructure supported by grant ANR-10-INBS-04 from the French National Research Agency. We also thank Jean-Michel Camadro and Thibault Leger (IJM proteomics platform) for proteomics analysis. This work was supported by the ANR Jeune Chercheur (ANR0015TD), the ATIP-Avenir Program, the Foundation Schlumberger for the Education and Research (FSER) (FRM n°206548) and the Fondation Vaincre Alzheimer (FVA) (eOTP:669122 LS 212527) to F.G.; the Academy of Finland (grants 285223 and 322647), the Sigrid Jusélius Foundation, the Finnish Foundation for Cardiovascular Research, and the Magnus Ehrnrooth Foundation to V.M.O.; and the Association Française contre les Myopathies (AFM-Téléthon Research grants 20123 and 23778) and the ITMO-Inserm Plan Cancer 2014–2019 to D.T.

AUTHOR CONTRIBUTIONS

F.G. conceived and supervised the work. V.O. designed and supervised the radiometric assays for PS-to-PE conversion and the expression analysis by RT-PCR. D.T. designed and supervised the *in vitro* lipid transfer assays. L.R. performed and analyzed the cell experiments, including cell imaging and Seahorse analysis. V.C. performed and analyzed most of the cell experiments, including IF for endogenous proteins and Duolink. L.R., A.H., and F.G. performed and analyzed the EM experiments. C.S. participated in the setting up of the Seahorse experiments. C.S., A.H., and D.T. performed and analyzed the *in vitro* lipid transfer assays. A.A., E.J., and A.K. performed and analyzed the radiometric assays for PS-to-PE conversion. E.M., J.D., and J.S. performed MS-lipidomic analysis. R.L.B. provided tools and techniques for Duolink imaging analysis. J.N. and N.E.K. provided technical help in western blot analysis and generated some of the constructs for mammalian cell expression. V.C., L.R., and F.G. wrote the manuscript and all authors commented on the manuscript.

DECLARATION OF INTERESTS

The authors declare no competing interests.

Received: July 30, 2021
Revised: May 10, 2022
Accepted: August 24, 2022
Published: September 20, 2022

REFERENCES

Aaltonen, M.J., Friedman, J.R., Osman, C., Salin, B., di Rago, J.P., Nunnari, J., Langer, T., and Tatsuta, T. (2016). MICOS and phospholipid transfer by Ups2-Mdm35 organize membrane lipid synthesis in mitochondria. J. Cell Biol. *213*, 525–534.

Acoba, M.G., Senoo, N., and Claypool, S.M. (2020). Phospholipid ebb and flow makes mitochondria go. J. Cell Biol. *219*, e202003131.

Chen, H., Born, E., Mathur, S.N., and Field, F.J. (1993). Cholesterol and sphingomyelin syntheses are regulated independently in cultured human intestinal cells, CaCo-2: role of membrane cholesterol and sphingomyelin content. J. Lipid Res. *34*, 2159–2167.

Chung, J., Torta, F., Masai, K., Lucast, L., Czapla, H., Tanner, L.B., Narayanaswamy, P., Wenk, M.R., Nakatsu, F., and De Camilli, P. (2015). INTRACELLULAR TRANSPORT. PI4P/phosphatidylserine countertransport at ORP5- and ORP8-mediated ER-plasma membrane contacts. Science *349*, 428–432.

Ding, C., Wu, Z., Huang, L., Wang, Y., Xue, J., Chen, S., Deng, Z., Wang, L., Song, Z., and Chen, S. (2015). Mitofilin and CHCHD6 physically interact with Sam50 to sustain cristae structure. Sci. Rep. *5*, 16064.

Friedman, J.R., Mourier, A., Yamada, J., McCaffery, J.M., and Nunnari, J. (2015). MICOS coordinates with respiratory complexes and lipids to establish mitochondrial inner membrane architecture. Elife *4*.

Gallo, A., Danglot, L., Giordano, F., Hewlett, B., Binz, T., Vannier, C., and Galli, T. (2020). Role of the Sec22b-E-Syt complex in neurite growth and ramification. J. Cell Sci. *133*, jcs247148.

Galmes, R., Houcine, A., van Vliet, A.R., Agostinis, P., Jackson, C.L., and Giordano, F. (2016). ORP5/ORP8 localize to endoplasmic reticulum-mitochondria contacts and are involved in mitochondrial function. EMBO Rep. *17*, 800–810.

Gatta, A.T., and Levine, T.P. (2017). Piecing Together the Patchwork of Contact Sites. Trends Cell Biol. *27*, 214–229.

Ghai, R., Du, X., Wang, H., Dong, J., Ferguson, C., Brown, A.J., Parton, R.G., Wu, J.W., and Yang, H. (2017). ORP5 and ORP8 bind phosphatidylinositol-4, 5-biphosphate (PtdIns(4, 5)P 2) and regulate its level at the plasma membrane. Nat. Commun. *8*, 757.

Giordano, F. (2018). Non-vesicular lipid trafficking at the endoplasmic reticulum-mitochondria interface. Biochem. Soc. Trans. *46*, 437–452.

Giordano, F., Saheki, Y., Idevall-Hagren, O., Colombo, S.F., Pirruccello, M., Milosevic, I., Gracheva, E.O., Bagriantsev, S.N., Borgese, N., and De Camilli, P. (2013). PI(4, 5)P2-dependent and Ca(2+)-regulated ER-PM interactions mediated by the extended synaptotagmins. Cell *153*, 1494–1509.

Giordano, F., and Prodromou, C. (2021). The PTPIP51 TPR-domain: a novel lipid transfer domain? Contact *4*. 251525642110561–251525642110564.

Hanada, K., Nishijima, M., Kiso, M., Hasegawa, A., Fujita, S., Ogawa, T., and Akamatsu, Y. (1992). Sphingolipids are essential for the growth of Chinese hamster ovary cells. Restoration of the growth of a mutant defective in sphingoid base biosynthesis by exogenous sphingolipids. J. Biol. Chem. *267*, 23527–23533.

Harner, M., Körner, C., Walther, D., Mokranjac, D., Kaesmacher, J., Welsch, U., Griffith, J., Mann, M., Reggiori, F., and Neupert, W. (2011). The mitochondrial contact site complex, a determinant of mitochondrial architecture. EMBO J. *30*, 4356–4370.

Heikinheimo, L., and Somerharju, P. (1998). Preferential decarboxylation of hydrophilic phosphatidylserine species in cultured cells. Implications on the mechanism of transport to mitochondria and cellular aminophospholipid species compositions. J. Biol. Chem. *273*, 3327–3335.

Herrera-Cruz, M.S., and Simmen, T. (2017). Of yeast, mice and men: MAMs come in two flavors. Biol. Direct *12*, 3.

Hirabayashi, Y., Kwon, S.K., Paek, H., Pernice, W.M., Paul, M.A., Lee, J., Erfani, P., Raczkowski, A., Petrey, D.S., Pon, L.A., and Polleux, F. (2017). ER-mitochondria tethering by PDZD8 regulates Ca(2+) dynamics in mammalian neurons. Science *358*, 623–630.

Höhr, A.I.C., Lindau, C., Wirth, C., Qiu, J., Stroud, D.A., Kutik, S., Guiard, B., Hunte, C., Becker, T., Pfanner, N., and Wiedemann, N. (2018). Membrane protein insertion through a mitochondrial beta-barrel gate. Science *359*, eaah6834.

Hoppins, S., Collins, S.R., Cassidy-Stone, A., Hummel, E., Devay, R.M., Lackner, L.L., Westermann, B., Schuldiner, M., Weissman, J.S., and Nunnari, J. (2011). A mitochondrial-focused genetic interaction map reveals a scaffold-like complex required for inner membrane organization in mitochondria. J. Cell Biol. *195*, 323–340.

Huynen, M.A., Mühlmeister, M., Gotthardt, K., Guerrero-Castillo, S., and Brandt, U. (2016). Evolution and structural organization of the mitochondrial contact site (MICOS) complex and the mitochondrial intermembrane space bridging (MIB) complex. Biochim. Biophys. Acta *1863*, 91–101.

John, G.B., Shang, Y., Li, L., Renken, C., Mannella, C.A., Selker, J.M.L., Rangell, L., Bennett, M.J., and Zha, J. (2005). The mitochondrial inner membrane protein mitofilin controls cristae morphology. Mol. Biol. Cell *16*, 1543–1554.

Joshi, A.S., Thompson, M.N., Fei, N., Hüttemann, M., and Greenberg, M.L. (2012). Cardiolipin and mitochondrial phosphatidylethanolamine have overlapping functions in mitochondrial fusion in Saccharomyces cerevisiae. J. Biol. Chem. *287*, 17589–17597.

Kawano, S., Tamura, Y., Kojima, R., Bala, S., Asai, E., Michel, A.H., Kornmann, B., Riezman, I., Riezman, H., Sakae, Y., et al. (2018). Structure-function insights into direct lipid transfer between membranes by Mmm1-Mdm12 of ERMES. J. Cell Biol. *217*, 959–974.

Kim, H., Lee, S., Jun, Y., and Lee, C. (2022). Structural basis for mitoguardin-2 mediated lipid transport at ER-mitochondrial membrane contact sites. Nat. Commun. *13*, 3702.

Kim, S.H., Song, H.E., Kim, S.J., Woo, D.C., Chang, S., Choi, W.G., Kim, M.J., Back, S.H., and Yoo, H.J. (2017). Quantitative structural characterization of phosphatidylinositol phosphates from biological samples. J. Lipid Res. *58*, 469–478.

Körner, C., Barrera, M., Dukanovic, J., Eydt, K., Harner, M., Rabl, R., Vogel, F., Rapaport, D., Neupert, W., and Reichert, A.S. (2012). The C-terminal domain of Fcj1 is required for formation of crista junctions and interacts with the TOB/SAM complex in mitochondria. Mol. Biol. Cell *23*, 2143–2155.

Kornmann, B., Currie, E., Collins, S.R., Schuldiner, M., Nunnari, J., Weissman, J.S., and Walter, P. (2009). An ER-mitochondria tethering complex revealed by a synthetic biology screen. Science *325*, 477–481.

Kozjak, V., Wiedemann, N., Milenkovic, D., Lohaus, C., Meyer, H.E., Guiard, B., Meisinger, C., and Pfanner, N. (2003). An essential role of Sam50 in the protein sorting and assembly machinery of the mitochondrial outer membrane. J. Biol. Chem. *278*, 48520–48523.

Kozjak-Pavlovic, V., Ross, K., Benlasfer, N., Kimmig, S., Karlas, A., and Rudel, T. (2007). Conserved roles of Sam50 and metaxins in VDAC biogenesis. EMBO Rep. *8*, 576–582.

Kumar, N., Leonzino, M., Hancock-Cerutti, W., Horenkamp, F.A., Li, P., Lees, J.A., Wheeler, H., Reinisch, K.M., and De Camilli, P. (2018). VPS13A and VPS13C are lipid transport proteins differentially localized at ER contact sites. J. Cell Biol. *217*, 3625–3639.

Lang, A., John Peter, A.T., and Kornmann, B. (2015). ER-mitochondria contact sites in yeast: beyond the myths of ERMES. Curr. Opin. Cell Biol. *35*, 7-12.

Liebisch, G., Lieser, B., Rathenberg, J., Drobnik, W., and Schmitz, G. (2004). High-throughput quantification of phosphatidylcholine and sphingomyelin by electrospray ionization tandem mass spectrometry coupled with isotope correction algorithm. Biochim. Biophys. Acta *1686*, 108–117.

Maeda, K., Anand, K., Chiapparino, A., Kumar, A., Poletto, M., Kaksonen, M., and Gavin, A.C. (2013). Interactome map uncovers phosphatidylserine transport by oxysterol-binding proteins. Nature *501*, 257–261.

Olkkonen, V.M. (2015). OSBP-related protein family in lipid transport over membrane contact sites. Lipid Insights *8*, 1–9.

Ott, C., Dorsch, E., Fraunholz, M., Straub, S., and Kozjak-Pavlovic, V. (2015). Detailed analysis of the human mitochondrial contact site complex indicate a hierarchy of subunits. PLoS One *10*, e0120213.

Ott, C., Ross, K., Straub, S., Thiede, B., Götz, M., Goosmann, C., Krischke, M., Mueller, M.J., Krohne, G., Rudel, T., and Kozjak-Pavlovic, V. (2012). Sam50 functions in mitochondrial intermembrane space bridging and biogenesis of respiratory complexes. Mol. Cell Biol. *32*, 1173–1188.

Schikorski, T., Young, S.M., Jr., and Hu, Y. (2007). Horseradish peroxidase cDNA as a marker for electron microscopy in neurons. J. Neurosci. Methods *165*, 210–215.

Scorrano, L., De Matteis, M.A., Emr, S., Giordano, F., Hajnóczky, G., Kornmann, B., Lackner, L.L., Levine, T.P., Pellegrini, L., Reinisch, K., et al. (2019). Coming together to define membrane contact sites. Nat. Commun. *10*, 1287.

Shiao, Y.J., Lupo, G., and Vance, J.E. (1995). Evidence that phosphatidylserine is imported into mitochondria via a mitochondria-associated membrane and that the majority of mitochondrial phosphatidylethanolamine is derived from decarboxylation of phosphatidylserine. J. Biol. Chem. *270*, 11190–11198.

Shibata, Y., Voss, C., Rist, J.M., Hu, J., Rapoport, T.A., Prinz, W.A., and Voeltz, G.K. (2008). The reticulon and DP1/Yop1p proteins form immobile oligomers in the tubular endoplasmic reticulum. J. Biol. Chem. *283*, 18892–18904.

Slot, J.W., and Geuze, H.J. (2007). Cryosectioning and immunolabeling. Nat. Protoc. *2*, 2480–2491.

Steenbergen, R., Nanowski, T.S., Beigneux, A., Kulinski, A., Young, S.G., and Vance, J.E. (2005). Disruption of the phosphatidylserine decarboxylase gene in mice causes embryonic lethality and mitochondrial defects. J. Biol. Chem. *280*, 40032–40040.

Stoica, R., De Vos, K.J., Paillusson, S., Mueller, S., Sancho, R.M., Lau, K.F., Vizcay-Barrena, G., Lin, W.L., Xu, Y.F., Lewis, J., et al. (2014). ER-mitochondria associations are regulated by the VAPB-PTPIP51 interaction and are disrupted by ALS/FTD-associated TDP-43. Nat. Commun. *5*, 3996.

Tamura, Y., Kawano, S., and Endo, T. (2020). Lipid homeostasis in mitochondria. Biol. Chem. *401*, 821–833.

Tang, J., Zhang, K., Dong, J., Yan, C., Hu, C., Ji, H., Chen, L., Chen, S., Zhao, H., and Song, Z. (2020). Sam50-Mic19-Mic60 axis determines mitochondrial cristae architecture by mediating mitochondrial outer and inner membrane contact. Cell Death Differ. *27*, 146–160.

Tasseva, G., Bai, H.D., Davidescu, M., Haromy, A., Michelakis, E., and Vance, J.E. (2013). Phosphatidylethanolamine deficiency in Mammalian mitochondria impairs oxidative phosphorylation and alters mitochondrial morphology. J. Biol. Chem. *288*, 4158–4173.

Tatsuta, T., Scharwey, M., and Langer, T. (2014). Mitochondrial lipid trafficking. Trends Cell Biol. *24*, 44–52.

van der Laan, M., Horvath, S.E., and Pfanner, N. (2016). Mitochondrial contact site and cristae organizing system. Curr. Opin. Cell Biol. *41*, 33–42.

Vance, J.E. (1990). Phospholipid synthesis in a membrane fraction associated with mitochondria. J. Biol. Chem. *265*, 7248–7256.

Vance, J.E. (2014). MAM (mitochondria-associated membranes) in mammalian cells: lipids and beyond. Biochim. Biophys. Acta *1841*, 595–609.

Vance, J.E., and Tasseva, G. (2013). Formation and function of phosphatidylserine and phosphatidylethanolamine in mammalian cells. Biochim. Biophys. Acta *1831*, 543–554.

von der Malsburg, K., Müller, J.M., Bohnert, M., Oeljeklaus, S., Kwiatkowska, P., Becker, T., Loniewska-Lwowska, A., Wiese, S., Rao, S., Milenkovic, D., et al. (2011). Dual role of mitofilin in mitochondrial membrane organization and protein biogenesis. Dev. Cell *21*, 694–707.

Wang, H., Ma, Q., Qi, Y., Dong, J., Du, X., Rae, J., Wang, J., Wu, W.F., Brown, A.J., Parton, R.G., et al. (2019). ORP2 delivers cholesterol to the plasma membrane in exchange for phosphatidylinositol 4, 5-bisphosphate (PI(4, 5)P2). Mol. Cell *73*, 458–473.e7.

Wideman, J.G., Balacco, D.L., Fieblinger, T., and Richards, T.A. (2018). PDZD8 is not the 'functional ortholog' of Mmm1, it is a paralog. F1000Res. *7*, 1088.

Wollweber, F., von der Malsburg, K., and van der Laan, M. (2017). Mitochondrial contact site and cristae organizing system: a central player in membrane shaping and crosstalk. Biochim. Biophys. Acta. Mol. Cell Res. *1864*, 1481–1489.

Wong, L.H., Gatta, A.T., and Levine, T.P. (2019). Lipid transfer proteins: the lipid commute via shuttles, bridges and tubes. Nat. Rev. Mol. Cell Biol. *20*, 85–101.

Yeo, H.K., Park, T.H., Kim, H.Y., Jang, H., Lee, J., Hwang, G.S., Ryu, S.E., Park, S.H., Song, H.K., Ban, H.S., et al. (2021). Phospholipid transfer function of PTPIP51 at mitochondria-associated ER membranes. EMBO Rep. *22*, e51323.

STAR★METHODS

KEY RESOURCES TABLE

REAGENT or RESOURCE	SOURCE	IDENTIFIER
Antibodies		
Mouse monoclonal anti-beta-actin	Abcam	ab8226
Mouse monoclonal anti-GFP	Roche	11814460001
Rabbit polyclonal anti-GFP	ThermoFisher	A-11122
Mouse monoclonal anti-HA	Sigma Aldrich	H3663
Mouse monoclonal anti-IP3R-3	BD Transduction Laboratories	610312
Mouse monoclonal anti-metaxin2	Santa Cruz	514231
Rabbit polyclonal anti-Mic60	Proteintech	10179-1-AP
Rabbit polyclonal anti-ORP5	Sigma Aldrich	HAP038712
Rabbit polyclonal anti-ORP5	Sigma Aldrich	HPA058727
Rabbit polyclonal anti-ORP8	GeneTex	GTX121273
Mouse monoclonal anti-ORP8	Santa Cruz	134409
Rabbit polyclonal anti-PDI	GeneTex	GTX101468
Rabbit polyclonal anti-PISD	Sigma Aldrich	HPA031090
Rabbit polyclonal anti-PSS1	Sigma Aldrich	HPA016852
Rabbit polyclonal anti-SAMM50	Sigma Aldrich	HPA034537
Mouse monoclonal anti-TOM20	BD Transduction Laboratories	612278
Rabbit polyclonal anti-VAPB	Sigma Aldrich	HPA013144
Goat anti-rabbit Alexa Fluor 488	Invitrogen	A-11008
Goat anti-mouse Alexa Fluor 488	Invitrogen	A-21121
Goat anti-mouse Alexa Fluor 555	Invitrogen	A-21422
Donkey anti-rabbit Ig – HRP	GE Healthcare	Nv934V
Sheep anti-mouse Ig – HRP	GE Healthcare	Nv931V
Bacterial and virus strains		
One Shot™ TOP10 Chemically Competent *E. coli*	Invitrogen	C404010
One Shot™ BL21(DE3) Chemically Competent *E. coli*	Invitrogen	C6000003
Chemicals, peptides, and recombinant proteins		
Cocodylate	Electron Microscopy Sciences	11652
3,3′-Diaminobenzidine (DAB)	Sigma Aldrich	D8001
Gluteraldehyde	Electron Microscopy Sciences	16220
Paraformaldheyde (PFA)	Electron Microscopy Sciences	15710
Percoll	Sigma Aldrich	P1644
Rotenone/Antimycin A	Sigma Aldrich	A8674
Oligomycin	Sigma Aldrich	O4876
Carbonyl cyanide 4-(trifluoromethoxy) phenylhydrazone (FCCP)	Cayman Chemical	15218
Protein assay dye reagent concentrate	Bio-Rad	500-0006
Pierce BCA protein assay	Thermo Fisher Scientific	23227
Hydroxylamine HCL	Sigma	25,558-0
β-chloro-L-alanine	Sigma	C9033
4–20% Mini-PROTEAN® TGX™ Precast Protein Gels, 10-well	Bio-Rad	4561094

(*Continued on next page*)

Continued

REAGENT or RESOURCE	SOURCE	IDENTIFIER
4–15% Mini-PROTEAN® TGX™ Precast Protein Gels, 12-well	Bio-Rad	4561085
Amersham™ Protran® Western blotting membranes, nitrocellulose	GE Healthcare	10600016
Gibco™ DMEM, high glucose, GlutaMAX™ Supplement, pyruvate	Gibco™	31966021
Gibco™ Trypsin-EDTA (0.05%), phenol red	Gibco™	25300054
Gibco™ Penicillin-Streptomycin (10,000 U/mL)	Gibco™	15140122
Gibco™ Opti-MEM™ I Reduced Serum Medium, GlutaMAX™ Supplement	Gibco™	51985026
Gibco™ Fetal Bovine Serum, qualified, Brazil	Gibco™	10270106
cOmplete™, Mini, EDTA-free Protease Inhibitor Cocktail	Roche	1183617001
Chromotek GFP-Trap Agarose beads	Allele Biotech	gta-20
Oligofectamine	Invitrogen	12252011
Lipofectamine™ 2000 Transfection Reagent	Invitrogen	11668019
MitoTracker® Red	Invitrogen	M7512
SYBR-Green I Master mix	Roche, Basel, Switzerland	04707516001
TopFluor® PC	Avanti Polar Lipids	810281C
TopFluor® PS	Avanti Polar Lipids	810283C
TopFluor® PE	Avanti Polar Lipids	810282C
Biotinyl Cap PE	Avanti Polar Lipids	
POPC	Avanti Polar Lipids	850457C
Streptavidin-coated magnetic beads (DynabeadsMyOne Streptavidin T1)	Invitrogen	65601
n-dodecyl-β-D-Maltose (DDM)	EDM Millipore	324355
Critical commercial assays		
PureLink™ RNA Mini Kit	Ambion / Thermo Fisher Scientific	12183018A
SuperScript VILO™ cDNA synthesis KIT	Invitrogen/ Thermo Fisher Scientific	11754050
Duolink® In Situ Detection Reagents Green	Sigma	DUO92002
Duolink® In Situ Detection Reagents Red	Sigma	DUO92008
Duolink® In Situ PLA® Probe Anti-Rabbit PLUS	Sigma	DUO92014
Duolink® In Situ PLA® Probe Anti-Mouse MINUS	Sigma	DUO92004
Duolink® In Situ Mounting Medium with DAPI	Sigma	DUO82040
Amersham™ ECL™ Select Western Blotting Detection Reagent	cytiva	RPN2235
Experimental models: Cell lines		
Human: HeLa cells	from P. De Camilli (Giordano et al. 2013)	ATCC
Oligonucleotides		
siRNAs targeting ORP5	Galmes et al., 2016	Dharmacon, J-009274-10 and Dharmacon, J-009274-11
siRNAs targeting ORP8	Galmes et al., 2016	Dharmacon, J-009508-06 and Dharmacon, J-009508-05
siRNAs targeting SAM50	Dharmacon	J-017871-18 and J-017871-19

(*Continued on next page*)

Continued

REAGENT or RESOURCE	SOURCE	IDENTIFIER
siRNA targeting Mic60: 5′AAUUGCUGGAGCUGGCCUUTT-3′	John et al., 2005	
Non-targeting siRNA	Dharmacon	D-001810-10
Primer ORP5 forward (qPCR): 5′-GTGCCGCTGGAGGAGCAGAC-3′	This paper	N/A
Primer ORP5 reverse (qPCR): 5′-AGGGGCTGTGGTCCTCGTATC-3′	This paper	N/A
Primer SAMM50 forward (qPCR): 5′-CAAGTGGACCTGATTTTGGAGG-3′	This paper	N/A
Primer SAMM50 reverse (qPCR): 5′-AGACGGAGCAATTTTTCACGG-3′	This paper	N/A
Primer Mic60 forward (qPCR): 5′-GTTGTATCTCAGTATCATGAGCTGG-3′	This paper	N/A
Primer Mic60 reverse (qPCR): 5′-GTTCAGCTGATCAATACGACGA-3′	This paper	N/A
Primer cloning HA-ORP5 forward: 5′-GGCGGC*ACCGGT*cgccaccATGTAC CCATCGATGTTCCAGATTACGCTatg aaggaggaggccttcctc-3′	This paper	N/A
Primer cloning HA-ORP5 reverse: 3′-GGC*CTCGAG*ctatttgaggatgtggttaatg-5′	This paper	N/A
Primer cloning Mic60-GFP forward: 5′-AGACCCAAGCTT *GGTACC* atg -3′	This paper	N/A
Primer cloning Mic60-GFP forward: 3′-GTAATC*GGATTC* GC ctctggct-5′	This paper	N/A
Primer cloning ORD5 forward: 5′-GCACAG GTCGAC TCgagacccctggggccccggt-3′	This paper	N/A
Primer cloning ORD5 ORD: 3′-GCACA*GCGGCCGC*ctactgtggc cggagggctggtcg-5′	This paper	N/A
Recombinant DNA		
EGFP-ORP5	Galmes et al., 2016	N/A
EGFP-ORP8	Galmes et al., 2016	N/A
EGFP-ORP5ΔPH	Galmes et al., 2016	N/A
EGFP-ORP8ΔPH	Galmes et al., 2016	N/A
EGFP-ORP5ΔORD	Galmes et al., 2016	N/A
EGFP-ORP5ΔTM	Galmes et al., 2016	N/A
RFP-Sec22b	Gallo et al., 2020	N/A
GFP-Sec61β	Harward University (Shibata et al., 2008)	N/A
PHPLCδ-RFP	Chung et al., 2015	N/A
Mito-BFP	Addgene	49,151
ssHRP-KDEL	Schikorski et al., 2007	N/A
GST-ORD8	from P. De Camilli (Chung et al., 2015)	N/A
GST-ORD5	This paper	N/A
HA-ORP5	This paper	N/A
Mic60-GFP	This paper	N/A
FLAG-Mic60	Ott et al., 2015	N/A
pEGFP-C1 vector	Clontech	N/A
pEGFP-N1 vector	Clontech	N/A

(*Continued on next page*)

Continued

REAGENT or RESOURCE	SOURCE	IDENTIFIER
Software and algorithms		
Image J	National Institutes of Health, USA	https://imagej.nih.gov/ij/
GraphPad Prism 9.0	GraphPad Software	https://www.graphpad.com/scientific-software/prism/
Exel Microsoft Office 16.57	Microsoft Corporation	https://www.microsoft.com/
Imaris V 9.3	Bitplane	https://imaris.oxinst.com/
Image Lab™ software 6.0	Bio-Rad Laboratories	https://www.bio-rad.com/

RESOURCE AVAILABILITY

Lead contact

Further information and requests for resources and reagents should be directed to and will be fulfilled by the lead contact, Francesca Giordano (francesca.giordano@i2bc.paris-saclay.fr).

Materials availability

All unique reagents generated in this study are available from the lead contact upon request.

Data and code availability

- The data reported in this paper will be shared by the lead contact uponrequest.
- This paper does not report original code.
- Any additional information required to reanalyze the data reported in this paper is available from the lead contact upon request.

EXPERIMENTAL MODEL AND SUBJECT DETAILS

Cell line

HeLa cells were used for KD, transfection, biochemistry, light and electron microscopy, and lipidomic studies. HeLa cells were cultured in Dulbecco's Modified Eagle Medium (DMEM, Life Technologies) supplemented with 10% FBS (Life Technologies) and 1% penicillin/streptomycin (P/S, 100 units/mL penicillin and 10 μg/mL streptomycin, Life Technologies) and maintained at 37°C with 5% CO_2.

METHOD DETAILS

cDNA plasmids and molecular cloning

EGFP-ORP5, EGFP-ORP8, EGFP-ORP5ΔPH, EGFP-ORP8ΔPH, EGFP-ORP5ΔORD and EGFP-ORP5ΔTM were described in (Galmes et al., 2016) and RFP-Sec22b in (Gallo et al., 2020). The following reagents were kind gifts: GFP-Sec61β from T. Rapoport (Harward University) (Shibata et al., 2008), PHPLCδ-RFP (Chung et al., 2015); Mito-BFP (Addgene: # 49151); ssHRP-KDEL from T. Schikorski (Schikorski et al., 2007); GST-ORD8 (ORD ORP8, corresponding to aa 328–767) from P. De Camilli (Chung et al., 2015).

Cloning of HA-ORP5, Mic60-GFP and GST-ORD5 (ORD ORP5): cDNAs of ORP5 (full-length), Mic60 (full-length from FLAG-Mic60 (Ott et al., 2015) and GST-ORD5 (corresponding to aa 265–703), were amplified by PCR. In all PCR reactions, Herculase II fusion DNA polymerase (Agilent) was used.

Primers used were (coding sequence shown in lowercase):

5′ AgeI-HA-ORP5_Fw GGCGGC *ACCGGT* cgccacc ATGTACCCATACGATGTTCCA GATTACGCT atgaaggaggaggccttcctc
3′ XhoI-STOP-ORP5_Rv GGC *CTCGAG* ctatttgaggatgtggttaatg
5′ KpnI- Mic60_Fw AGACCCAAGCTT *GGTACC* atg.
3′ BamHI-GC- Mic60_Rv GTAATC *GGATTC* GC ctctggct
5′ SalI-TC-ORD5_Fw GCACAG GTCGAC TC gagacccctggggccccggt
3′ NotI-STOP-ORD5_Rv GCACA *GCGGCCGC* ctactgtggccggagggctggtcg

For HA-ORP5 cloning, the PCR product (carrying the HA tag at the N-terminus of ORP5) was ligated between AgeI and XhoI in the pEGFP-C1 vector (Clontech) and replacing the GFP-tag was replaced with the HA-tag. For the other clonings the PCR products were ligated between KpnI and BamHI for Mic60, and between SalI and NotI for ORD5, in the pEGFP-N1 vector (Clontech) to generate Mic60-EGFP or in the pGEX-6P-1 to generate GST-ORD5.

Cell transfection

HeLa cells were seeded in 13mm glass coverslips (Agar Scientific) or in 10 cm dishes, were transfected with 1 μg or 24 ug DNA, respectively, using Lipofectamine2000 (Invitrogen) according to the manufacturer's instruction. Cells were cultured for 24 h prior to analysis.

RNA interference

ORP5, ORP8, SAM50 and Mic60 KD in Hela cells was achieved by siRNA transfection. HeLa cells were seeded in 13 mm coverslips (Agar Scientific) or in 10 cm dishes transfected with 200 nM siRNA using Oligofectamine (Invitrogen) following the manufacturer's instruction. Cells were cultured for 48 h prior to analysis. Double-stranded siRNAs were derived from the following references: OSBPL8 Dharmacon, J-009508-06 (Galmes et al., 2016); OSBPL8 Dharmacon, J-009508-05 (Galmes et al., 2016); OSBPL5 Dharmacon, J-009274-10 (Galmes et al., 2016); OSBPL5 Dharmacon, J-009274-11(Galmes et al., 2016); SAMM50 Dharmacon, J-017871-18; SAMM50 Dharmacon, J-017871-19; Mic60 5′AAUUGCUGGAGCUGGCCUUTT-3′ (John et al., 2005); non-targeting Dharmacon, D-001810-10.

mRNA analyses by quantitative reverse transcriptase PCR (qPCR)

Total RNA was isolated from HeLa cells transfected with siRNAs for 48 h as described above, by using a Purelink™ kit (Ambion/Thermo Scientific, Foster City, CA). The RNA (0.5 μg per specimen) was reverse transcribed with a SuperScript VILO™ cDNA synthesis kit (Invitrogen/Thermo Scientific, Carlsbad, CA) according to the manufacturer's protocol. Quantification of the mRNAs of interest was carried out on a Roche Lightcycler™ 480 II instrument by using SYBR-Green I Master mix (Roche, Basel, Switzerland) and primers specified in the Table below. Succinate dehydrogenase complex subunit A, the mRNA of which remained markedly stable under the present conditions, was employed as a reference housekeeping mRNA. Relative mRNA levels were calculated by using the –ΔΔCt method.

Sequences of the primers used for qPCR:
SDHA (succinate dehydrogenase complex subunit A, housekeeping):
Fw: 5′-CATGCTGCCGTGTTCCGTGTGGG-3′,
Rv:3′-GGACAGGGTGTGCTTCCTCCAGTGCTCC-5‘;
ORP5:
Fw: 5′- GTGCCGCTGGAGGAGCAGAC′3′,
Rv: 3′-AGGGGCTGTGGTCCTCGTATC-5‘;
SAMM50:
Fw: 5′-CAAGTGGACCTGATTTTGGAGG-3′,
Rv: 3′-AGACGGAGCAATTTTTCACGG-5′,
Mic60:
Fw: 5′-GTTGTATCTCAGTATCATGAGCTGG-3′,
Rv: 3′-GTTCAGCTGATCAATACGACGA-5‘.

Immunoprecipitation of ORPs

HeLa cells transfected with EGFP-tagged ORPs were washed in cold PBS and lysed on ice in lysis buffer [50 mM Tris, 120 mM NaCl, 40 mM Hepes, 0.5% digitonin, 0.5% CHAPS, pH 7.36, and protease inhibitor cocktail (Roche)]. Cell lysates were then centrifuged at 21 000 g for 20 min at 4°C. Supernatants were then incubated with Chromotek GFP-trap agarose beads (Allele Biotech) for 1 h at 4°C under rotation. Subsequently beads were washed in 0.1 M phosphate buffer. After extensive washes in cold lysis buffer, immunoprecipitated proteins bound to the beads were processed for Mass Spectrometry analysis or incubated in sample buffer (containing 2% SDS) and then boiled for 1 min at 97°C. In the latter case immunoprecipitates were loaded and separated by 10% SDS–PAGE and immunoblotting was carried out.

Western blotting

For immunoblotting, cells were resuspended in lysis buffer [50 mM Tris, 150 mM NaCl, 1% Triton X-100, 10 mM EDTA, pH 7.2, and protease inhibitor cocktail (Roche)]. Cell lysates were then centrifuged at 21 000 g for 20 min at 4°C. The supernatants were boiled in reducing SDS sample buffer. Proteins isolated from HeLa cells or obtained by immunoprecipitation were subjected to separation by SDS-PAGE. The separated proteins were transferred to 0.45 μm Nitrocellulose membrane (GE Healthcare). The membrane was blocked by 5% non-fat milk in TBST buffer (TBS buffer with 0.1% Tween 20) for 1 h at room temperature and washed 3 times, for 5 min each, with TBST. Then the membrane was incubated with the primary antibodies (antibodies and dilutions listed below) at 4°C overnight. The membrane was washed 3 times with TBST incubated with the peroxidase-conjugated anti-rabbit IgG secondary antibody (1:10.000, in 5% milk in TBST) or anti-mouse IgG secondary (1:10.000, in 5% milk in TBST) at room temperature for 1 h, followed with washing and detection using the enhanced chemiluminescence (ECL) detection kit (Cytiva). For Western blot quantification, bands of protein of interest were detected using ChemiDoc™ Imaging Systems (Life Science Research, Bio-Rad) and analyzed using Image Lab™ Software. All data are presented as mean ± standard error of the mean (SEM) of three experimental replicates.

Antibodies and the respective working dilutions were as follows: IP3R-3 (BD Transduction Laboratories, 610312) 1:2000; ORP5 (SIGMA, HPA038712) 1:1000; ORP5 (SIGMA, HPA058727) 1:1000; β-Actin (Abcam, ab8226) 1:1000; ORP8 (GeneTex, GTX121273)

1:1000; SAM50 (SIGMA, HPA034537) 1:1000; Mic60 (Proteintech, 10179-1-AP) 1:1000; metaxin 2 (Santa Cruz, sc-514231) 1:1000; TOM20 (BD Transduction Laboratories, 612278) 1:10000; PDI (GeneTex, GTX30716) 1:500; VAPB (SIGMA, HPA013144) 1:500; PSS1 (PTDSS1, SIGMA, HPA016852) 1:300; PISD (SIGMA, HPA031090) 1:300; GFP (Roche, 11814460001) 1:1000; anti-mouse-HRP (GE Healthcare, NA931V) 1:10000; anti-rabbit-HRP (GE Healthcare, NA934V) 1:10000.

Mass spectrometry-proteomic analysis

Mass Spectrometry (MS) analysis was carried out by the proteomics/mass spectrometry platform of IJM (http://www.ijm.fr/plateformes/spectrometrie-de-masse). Briefly, after washes with binding buffer, immunoprecipitations beads were rinsed with 100 μL of NH4HCO3 25 mmol/L. Proteins on beads were digested overnight at 37°C by sequencing grade trypsin (12.5 μg/mL; Promega Madison, Wi, USA) in 20 μL of NH4HCO3 25 mmol/L. Digests were analysed by an Orbitrap Fusion (Thermo Fisher Scientific, San Jose, CA) equipped with a Thermo Scientific EASY-Spray nanoelectrospray ion source and coupled to an Easy nano-LC Proxeon 1000 system (Thermo Fisher Scientific, San Jose, CA). MS/MS data were processed with Proteome Discoverer 1.4 software (Thermo Fisher scientific, San Jose, CA) coupled to an in-house Mascot search server (Matrix Science, Boston, MA; version 2.4.2). MS/MS data were searched against SwissProt databases with Homo sapiens taxonomy. The Mascot score for a protein is the summed score for the individual peptides, e.g. peptide masses and peptide fragment ion masses, for all peptides matching a given protein. For a positive protein identification, the mascot score has to be above the 95% confidence level. In Mascot, the ions score for an MS/MS match is based on the calculated probability, P, that the observed match between the experimental data and the database sequence is a random event. The reported score is $-10\mathrm{Log}_{10}(P)$. A score of 200 indicates a probability of 10^{-20}. Scores greater than 70 are significant, while scores lower than 40 should not be considered or carefully validated at MS/MS level (source: http://www.matrixscience.com/help/interpretation_help.html). We thus set up a Mascot score threshold of 50.

Cell fractionation

HeLa cells (100×10^6 cells) were harvested 48 h after transfection with siRNA oligos and washed with PBS by centrifugation at 600 g for 5 min. The cell pellet was resuspended in starting buffer (225 mM mannitol, 75 mM sucrose and 30 mM Tris-HCl pH 7.4) and homogenized using a Tissue Grinder Dura-Grind®, Stainless Steel, Dounce (Wheaton). The homogenate was centrifuged three times at 600 g for 5 min to remove nuclei and unbroken cells. The crude mitochondria was pelleted by centrifugation at 10 000 g for 10 min. To separate MAM and pure mitochondria fractions, the pellet was resuspended in MRB buffer (250 mM mannitol, 5 mM HEPES and 0.5 mM EGTA, pH 7.4) and layered on top of different concentrations of Percoll gradient (225 mM mannitol, 25 mM HEPES, 1 mM EGTA pH 7.4 and 30% or 15% Percoll). After centrifugation at 95 000 g for 30 min, two dense bands containing either the pure mitochondria or MAM fraction were recovered and washed twice with MRB buffer by centrifugation at 6300 g for 10 min to remove residual Percoll and residual contamination. MAM was pelleted by centrifugation at 100 000 g for 1 h. MAMs and pure mitochondria pellets were resuspended in Lysis Buffer (50 mM Tris, 150 mM NaCl, 1% Triton X-100, 10 mM EDTA, pH 7.2, and protease inhibitor cocktail) and protein concentrations were determined by Bradford assay. Equal amounts of proteins were loaded on 4–20% gradient SDS-PAGE (Biorad) and immunoblotting was carried out. Pure mitochondria were processed for MS-lipidomic analysis.

Mass spectrometry-lipidomic analysis

700 μL of homogenized cells were mixed with 800 μL 1 N HCl:CH_3OH 1:8 (v/v), 900 μL $CHCl_3$ and 200 μg/mL of the antioxidant 2,6-di-tert-butyl-4-methylphenol (BHT; Sigma Aldrich). The organic fraction was evaporated using a Savant Speedvac spd111v (Thermo Fisher Scientific). Lipid pellets were reconstituted in running solution (CH_3OH:$CHCl_3$:NH_4OH; 90:10:1.25; v/v/v). Phospholipid species were analyzed by electrospray ionization tandem mass spectrometry (ESI-MS/MS) on a hybrid triple quadrupole/linear ion trap mass spectrometer (4000 QTRAP system; Applied Biosystems SCIEX) equipped with a TriVersa NanoMate (Advion Biosciences) robotic nanosource. Phospholipid profiling was executed by (positive or negative) precursor ion or neutral loss scanning at a collision energy of 35 eV for neutral loss of 141 Da (phosphatidylethanolamine (PE)). Phospholipid quantification was performed by multiple reaction monitoring (MRM), the transitions being based on the neutral losses or the typical product ions as described above. The MRM dwell time was set to 100 ms and typically the signal was averaged over 20 cycles. Lipid standards used were PE25:0 and PE43:6 (Avanti Polar Lipids). The data were corrected for isotope effects as described by (Liebisch et al., 2004).

Immunofluorescence

HeLa cells were seeded on 13 mm glass bottom coverslips (Agar Scientific). KD and/or transfected cells were incubated with 1 μM MitoTracker (mitochondrial marker, Invitrogen) for 30 min at 37°C, 5% CO_2 and then fixed with 4% PFA/PBS for 15 min at room temperature. Fixed cells were then washed in PBS and incubated with 50 mM NH4Cl/PBS for 15 min at room temperature. After washing with PBS and blocking buffer (1% BSA/0.1% Saponin in PBS), cells were incubated with primary antibodies diluted in blocking buffer for 1 h at room temperature and then with fluorescently-labeled secondary antibodies. After washing with blocking buffer and then PBS, coverslips were mounted on microscopy slides and images were acquired on Confocal inverted microscope SP8-X (DMI 6000 Leica). Optical sections were acquired with a Plan Apo 63× oil immersion objective (N.A. 1.4, Leica) using the LAS-X software. Fluorescence was excited using either a 405 nm laser diode or a white light laser, and later collected after adjusting the spectral windows with GaAsP PMTs or Hybrid detectors. Images from a mid-focal plane are shown. Images were processed and fluorescence was analysed off line using Image J. For co-localization analysis of fluorescent signals, the acquired images were processed using the

JACoP plugin in ImageJ to assess the Pearson's correlation coefficient. The obtained values, ranging from 0 to 1 (1 = max correlation), indicated the association between the signals analysed. To assess the distance between ORP5 or ORP8 and mitochondria confocal images were processed by Imaris, using a similar approach described in the PLA section. Antibodies and respective dilutions used for immunofluorescence were as follows: ORP5 (SIGMA, HPA038712) 1:150; ORP5 (SIGMA, HPA058727) 1:150; ORP8 (Santa Cruz, sc-134408) 1:200; ORP8 (GeneTex, GTX121273) 1:200; SAM50 (SIGMA, HPA034537) 1:100; HA (SIGMA, H3663) 1:800; Alexa Fluor 488 anti-rabbit (Invitrogen, A-11008) 1:500; Alexa Fluor 488 anti-mouse (Invitrogen, A-21121) 1:500; Alexa Fluor 555 anti-mouse (Invitrogen, A-21422) 1:500.

In situ proximity ligation assay (PLA)

The protein-protein interactions in fixed HeLa cells were assessed using *in situ* PLA (Duolink®SIGMA) according with the manufacturer's instructions. Briefly, HeLa cells seeded on 13 mm glass coverslips (Agar Scientific) were incubated with MitoTracker Red (mitochondrial marker, Invitrogen, 1 μM in DMEM) for 30 min at 37°C or co-transfected with PHPLCd-RFP (plasma membrane marker) plus Mito-BFP (mitochondrial marker). Cells were thereafter fixed with 4% PFA for 30 min at room temperature and incubated with primary antibodies (dilutions in the table below) in blocking solution (1% BSA, w/v, 0.01% saponin, w/v, in PBS) for 1hour at room temperature. PLUS and MINUS PLA probes (anti-murine and anti-rabbit IgG antibodies conjugated with oligonucleotides, 1:5 in blocking solution) were then incubated with the samples for 1hour at 37°C. Coverslips were thereafter washed in 1× wash buffer A and incubated with ligation solution (5× Duolink® Ligation buffer 1:5, ligase 1:40 in high purity water) for 30 min at 37°C. After the ligation step, cell samples were washed in 1× wash buffer A and incubated with the polymerase solution (5× Amplification buffer 1:5, polymerase 1:80 in high purity water) for 1hour 40min at 37°C. Polymerase solution was washed out from the coverslips with 1× wash buffer B and 0.01× wash buffer B. Vectashield Mounting Medium with or without DAPI (Vector Laboratories) was used for mounting. Images were acquired on Confocal inverted microscope SP8-X (DMI 6000 Leica). Optical sections were acquired with a Plan Apo 63× oil immersion objective (N.A. 1.4, Leica) using the LAS-X software. Fluorescence was excited using either a 405nm laser diode or a white light laser, and later collected after adjusting the spectral windows with GaAsP PMTs or Hybrid detectors. Images from a mid-focal plane or maximal projection of all layers are shown. Images were processed and the number and the distance of PLA dots to mitochondria and to the plasma membrane were assessed using the Imaris software (v 9.3, Bitplane). Briefly, segmented 3D images (PLA foci identified as ''spots'', mitochondria identified as ''surfaces'', and plasma membrane represented as ''cell'' were generated from confocal Z-stack images and the shortest distance between each spot center and the nearest point of the surface or cell object was calculated based on a 3D distance map. Spots objects (PLA dots) with a distance smaller than 380nm from surfaces (mitochondria) and cell (plasma membrane) objects were considered at a close proximity of these objects. The threshold of 380 nm was used as an estimation of the PLA reaction precision including both primary and secondary antibodies (30nm) plus half the FWHM of the PLA amplification signals (350nm). Antibodies and dilution used for PLA were as follows: ORP5 (SIGMA, HPA038712) 1:150; ORP8 (Santa Cruz,sc-134408) 1:150; ORP8 (GeneTex, GTX121273) 1:150; SAM50 (SIGMA, HPA034537) 1:200; metaxin 2 (Santa Cruz, sc-514231) 1:150; TOM20 (BD Transduction Laboratories, 612278) 1:150.

Electron microscopy analysis

Conventional EM

For conventional EM, cells grown on 13 mm glass bottom coverslips (Agar Scientific) were fixed with 2.5% glutaraldehyde and 2% PFA in 0.1 M cacodylate, 0.05% $CaCl_2$ buffer for 24 h. After several washes with 0.1 M cacodylate buffer, the cells were postfixed with 1% OsO_4, 1.5% potassium ferricyanide in 0.1M cacodylate for 1 h. After several washes with 0.1 M cacodylate buffer and H_2O, the cells were stained with 0.5% uranyl acetate for 24 h. After several washes with H_2O, the cells were dehydrated in ethanol and embedded in Epon while on the coverslips. Ultrathin sections were prepared, counterstained with uranyl acetate and observed under a MET JEOL 1400 equipped with a Orius High speed (Gatan) camera.

HRP detection

HeLa cells expressing HRP-KDEL were fixed on coverslips with 1.3% glutaraldehyde in 0.1 M cacodylate buffer, washed in 0.1 M ammonium phosphate [pH 7.4] buffer for 1 h and HRP was visualized with 0.5 mg/mL DAB and 0.005% H_2O_2 in 0.1 M Ammonium Phosphate [pH 7.4] buffer. Development of HRP (DAB dark reaction product) took between 5 min to 20 min and was stopped by extensive washes with cold water. Cells were postfixed in 2% OsO_4+1% $K_3Fe(CN)_6$ in 0.1 M cacodylate buffer for 1 h at 4°C, washed in cold water and then contrasted in 0.5% uranyl acetate for 2 h at 4°C, dehydrated in an ethanol series and embedded in epon as for conventional EM. Ultrathin sections were counterstained with 2% uranyl acetate and observed under a FEI Tecnai 12 microscope equipped with a CCD (SiS 1kx1k keenView) camera.

Immunogold labelling

HeLa cells were fixed with a mixture of 2%PFA and 0.125% glutaraldehyde in 0.1 M phosphate buffer [pH 7.4] for 2 h, and processed for ultracryomicrotomy as described previously (Slot and Geuze, 2007). Ultrathin cryosections were single- or double-immunogold-labeled with antibodies (GFP, Life technologies, A11122, 1:100; HA, SIGMA, H3663, 1:500; PDI, Genetex, GTX30716, 1:500) and protein A coupled to 10 or 15 nm gold (CMC, UMC Utrecht, The Netherlands), as indicated in the legends to the figures. Immunogold-labeled cryosections were observed under a FEI Tecnai 12 microscope equipped with a CCD (SiS 1kx1k keenView) camera.

For the quantification of the number of cristae junction in Epon sections, about 200 mitochondria were analyzed in randomly selected cell profiles and cristae junctions were counted in each of the mitochondria profile and reported as number of cristae/mitochondria profile. All data are presented as mean ± SEM of three experimental replicates.

For the quantification of ER-mitochondria contact sites in HRP-stained Epon sections, the total circumference of each mitochondria and the length of the multiple HRP-positive ER segments closely associated (<30 nm) with them were measured by manual drawing using the iTEM software (Olympus), as in (Galmes et al., 2016; Giordano et al., 2013), on acquired micrographs of HeLa cells for each cell profile, as indicated in the figure legends. Cells were randomly selected for analysis without prior knowledge of transfected plasmid or siRNA. All data are presented as mean (%) ±SEM of three experimental replicates.

For the quantifications of the total mitochondria surface the total circumference of each mitochondria was measured by manual drawing using the iTEM software (Olympus), and data are shown as average of total mitochondrial surface length (μm)/cell ±SD of three experimental replicates.

For the quantification of ORP5 immunogold labeling on ultrathin cryosections, 150 gold particles localized at ER-mitochondria contact sites were counted on acquired micrographs of randomly selected cell profiles at specific ranges of distance from CJ (0–50, 50–100, 100–150, 150–200 nm) in each of three experiments. All data are presented as mean (%) ±SEM of three technical replicates.

ORP5 and ORP8 ORD domain purification

Escherichia coli BL21DE3 RILP (Invitrogen) cells were transformed with plasmids encoding for GST tagged ORP5 (aa 265–703) or ORP8 (aa 328–767) ORD domains following the manufacturer's instruction. Bacteria were then grown overnight at 37°C and used to inoculate a large-scale volume (1L). When the OD_{600} reached 0.4, cultures were cooled down and incubated at 18°C until they reached O_{D600} = 0.65. Cells were induced by addition of isopropyl β-D-1-thiogalactopyranoside to a final concentration of 0.1 mM and incubated overnight at 18°C before harvesting. Cells were resuspended in 35 mL binding buffer (1X PBS, 1 mM EDTA, 1 mM DTT, Protease inhibitor) then 250 units of benzonase nuclease (Sigma) were added to the resuspension. Cells were lysed by sonication and the supernatant was recover after 20 min centrifugation at 184 000g and 4°C. Supernatant containing GST tagged proteins was incubated with 2 mL of Glutathione Sepharose 4 fast flow for 1 h at 4°C under nutation. Beads were washed using a series of wash buffers: 1st (1X PBS, 1 mM EDTA, 1 mM DTT), 2nd HSP-removal buffer (50 mM Tris pH 7.5, 50 mM KCl, 20 mM $MgCl_2$, 5 mM ATP) then cleavage buffer (50 mM Tris pH 7.5, 150 mM NaCl, 1 mM EDTA, 1 mM DTT). Cleavage of the GST tag was realized overnight at 4°C using Prescission protease. Untagged proteins were eluted with cleavage buffer, flash frozen and stored at −80°C until lipid transfer assay was performed.

Liposome preparation

1-palmitoyl-2-oleoyl-sn-glycero-3-phosphocholine (POPC), 1,2-dioleoyl-sn-glycero-3-phosphoethanolamine-N-(cap biotinyl) (Biotinyl Cap PE), 1-palmitoyl-2-(dipyrromethaneboron difluoride)undecanoyl-sn-glycero-3-phosphoethanolamine (TopFluor-PE), 1-palmitoyl-2-(dipyrromethaneboron difluoride)undecanoyl-sn-glycero-3-phospho-L-serine (TopFluor-PS), 1-palmitoyl-2-(dipyrromethaneboron difluoride)undecanoyl-sn-glycero-3-phosphocholine (TopFluor-PC) were purchased from Avanti Polar Lipids as chloroform solutions.

1 μmol of the appropriate lipid mixtures in chloroform solution was dried in a glass tube for 10 min under a gentle stream of argon, and then for 1 h under vacuum. The dried lipid films were resuspended in 1 mL of buffer H (25 mM HEPES/KOH, pH 7.7; 150 mM KCl; 10%(v/v) Glycerol) by vigorously vortexing for 30 min at room temperature. Unilamellar liposomes were produced by seven freeze-thaw cycles (30 s in liquid nitrogen followed by 5 min in a 37°C water bath) and extrusion (at least 21 times) through a polycarbonate filter with 100 nm pore size (polycarbonate membranes from Avanti Polar Lipids). The liposomes were then stored on ice.

Lipid transfer assay *in vitro*

The lipid transfer assays were realized with liposomes prepared as described above. The donor liposomes contained 1% mol TopFluor lipids (-PS, -PC or -PE) and 2% mol Biotinyl Cap PE and 97 mol% POPC. The acceptor liposomes contained only POPC. For each reaction, 25 μL of streptavidin-coated magnetic beads (DynabeadsMyOne Streptavidin T1, Invitrogen) were washed in buffer H and mixed with 25 μL of 1 mM donor liposomes. The mixture was incubated for 1 h at 25°C with intermittent gentle mixing. Bead-bound donor liposomes were then washed, resuspended in 25 μL and mixed with 25 μL of 1 mM acceptor liposomes and 50 μL of buffer H or protein (0.3 μM protein and 2.5 μM TopFluor lipids in the reaction solution). The mixture was incubated at 37°C for 1 h with intermittent gentle mixing. Supernatant containing acceptor liposomes was recovered after binding of bead-bound donor liposomes to a magnetic rack. TopFluor fluorescence of acceptor and donor liposomes was measured (after solubilization with 0.4% (w/v) n-dodecyl-β-D-maltoside, DDM) in a SpectraMax M5 plate reader (Molecular Device) equilibrated to 30°C (excitation: 450 nm; emission: 510 nm; cutoff: 475 nm; low gain). To confirm that fluorescence was transferred to acceptor liposomes, a fraction of the reaction supernatant – which has not been solubilized with DDM – was floated on a Nycodenz density gradient. 50 μL of supernatant was mixed with 100 μL of buffer H and 150 μL of Nycodenz 80% in buffer H. The solution was transferred to a 0.8 mL Ultra-Clear centrifuge tube (Beckman Coulter) and overlaid with 250 μL of Nycodenz 30% in buffer H and 75 μL of buffer H. The tubes were centrifuged in a SW 55 Ti rotor (Beckman Coulter) at 246,000 g for 4 h at 4°C. 50 μL were collected from the top of the gradient and the fluorescence was measured. The percentage of lipids transferred from donor to acceptor liposomes in the presence of ORD5 and ORD8 was determined using the following formula: $100*F_{acceptor}/(F_{acceptor} + F_{donor})$.

Radiometric assay for the conversion of PS to PE *in situ*

Radiometric assays without drugs

Hela cells were seeded on 6-well plates and transfected for 48 h with the non-targeting, ORP5 or ORP8-specific siRNAs specified above by using Oligofectamine (Thermo Fisher Scientific). The cells were then washed and shifted into Hanks balanced salt solution (Gibco) supplemented with a serine-free MEM amino acid mixture and MEM vitamins (Gibco), followed by 18 h labeling with 2 μL/well L-[^{3}H(G)]serine (30.9 Ci/mmol, NET24800, Perkin-Elmer) (Figure 6C). After the labeling (Figure 6C) or the chase (Figure 6D), the cells were scraped into 0.9 mL 2% NaCl per well, a 0.1 mL aliquot was withdrawn for protein analysis with the BCA assay (Thermo Fisher Scientific), and, after adding 50 nmol of unlabeled PS as carrier, the remaining 0.8 mL was subjected to lipid extraction by an acid modification of the Folch method (Kim et al., 2017). After drying, the lipids were resolved in 50 μL $CHCl_3$ and applied on Merck TLC Silica gel 60^{TM} plates, followed by separation by using $CHCl_3$-methanol-acetic acid-H2O (50:30:8:3.5) as solvent. The PS and PE spots identified from the mobility of standards run on the same plates were scraped into scintillation vials for analysis of [^{3}H] radioactivity. The DPM values were corrected for total cell protein, and the ratio of [^{3}H] in PE vs. PS calculated.

Radiometric assays with drugs

Post 48 h incubation of the cells with transfection complex, media was removed and cell monolayer was washed once with PBS and once with serum-free DMEM. Cells were incubated in a serum-free medium for 12 h. In some experiments, either β-chloro-L-alanine (1 mM) or Hydroxylamine (5 mM) was added to serum-free DMEM, 30 min prior to pulse, i.e after 11 h 30 min serum starvation, and cells were starved in serum-free DMEM containing the inhibitor for another 30 min. Cells were washed twice with PBS, and then incubated for 1 h at 37°C, CO_2 incubator in HBSS media containing 1X MEM amino acids and 1X MEM vitamins containing 7 μCi/mL of [^{3}H]serine. After the pulse, the cells were washed twice with PBS and chased for 4 h in serum-free DMEM at 37°C. The chase media also contained β-chloro-L-alanine (1 mM) or Hydroxylamine (5 mM). Samples were then washed twice with ice-cold PBS, scraped into 2% NaCl, and the lipids were extracted according to Bligh and Dyer. A fraction of each sample was lysed for protein estimation and blot as described above.

Mitochondrial respiration assay

Oxygen Consumption Rate (OCR) was measured using the XF_p Extracellular Flux Analyzer (Seahorse Bioscience Inc.). HeLa cells were seeded on a 6-well plate 3 days before the Seahorse experiment and KD of the proteins of interest was realized 2 days before. The day after KD, HeLa cells transfected with Ctrl, ORP5, or ORP8 siRNAs were plated in a Seahorse XFp 8-mini wells microplate. 20,000 HeLa cells were seeded in each well (except in the blank wells used for the background correction) in 180 μL of culture medium, and incubated overnight at 37° C in 5% CO2. One day after, the culture medium was replaced with 180 μL of XF DMEM Medium Solution pH 7.4 and then the 8-mini wells microplate was moved in a 37°C non-CO2 incubator before measurement. OCR was determined before drug additions and after addition of Oligomycin (1.5 μM), Carbonyl cyanide 4-(trifluoromethoxy) phenylhydrazone (FCCP, 0.5 μM), and Rotenone/Antimycin A (0.5 μM) (purchased from Agilent). After each assay, all the raw OCR data were analyzed using WAVE software.

QUANTIFICATIONS AND STATISTICAL ANALYSIS

Statistical analysis was performed with Microsoft Excel or GraphPad Prism 9.0. The data were presented as mean ± SEM. The n, indicated in the figures and figure legends, represent the total number of cells analyzed in three or more biological replicates, as stated in the figures legend. Statistical significance of two data sets were determined by unpaired student's t-test, with *$p < 0.05$, **$p < 0.01$, ***$p < 0.001$ and ****$p < 0.0001$.